

Evaluation of NU-WRF Performance on Air Quality Simulation under Various Model Resolutions – An Investigation within Framework of MICS-Asia Phase III

Zhining Tao^{1,2}, Mian Chin², Meng Gao³, Tom Kucsera^{1,2}, Dongchul Kim^{1,2}, Huisheng Bian^{2,4}, Jun-ichi Kurokawa⁵, Yuesi Wang⁶, Zirui Liu⁶, Gregory R. Carmichael⁷, Zifa Wang^{6,8,9}, and Hajime Akimoto¹⁰

1. Universities Space Research Association, Columbia, MD, USA
2. NASA Goddard Space Flight Center, Greenbelt, MD, USA
3. John A. Paulson School of Engineering and Applied Sciences, Harvard University, Cambridge, MA, USA
4. University of Maryland at Baltimore County, Baltimore, MD, USA
5. Japan Environmental Sanitation Center, Asia Center for Air Pollution Research, Niigata, 950-2144, Japan
6. State Key Laboratory of Atmospheric Boundary Layer Physics and Atmospheric Chemistry, Institute of Atmospheric Physics, Chinese Academy of Sciences, Beijing, 100029, China
7. Center for Global and Regional Environmental Research, University of Iowa, Iowa City, IA, USA
8. College of Earth Sciences, University of Chinese Academy of Sciences, Beijing, 100049, China
9. Center for Excellence in Urban Atmospheric Environment, Institute of Urban Environment, Chinese Academy of Sciences, Xiamen, 361021, China
10. National Institute for Environmental Studies, Onogawa, Tsukuba, 305-8506, Japan

1 **Abstract**

2
3
4
5
6
7
8
9
10
11
12
13
14
15
16
17
18
19
20
21
22
23
24
25
26
27

Horizontal grid resolution has a profound effect on model performances on meteorology and air quality simulations. In contribution to MICS-Asia Phase III, one of whose goals was to identify and reduce model uncertainty in air quality prediction, this study examined the impact of grid resolution on meteorology and air quality over East Asia, focusing on the North China Plain (NCP) region. NASA Unified Weather Research and Forecasting (NU-WRF) model has been applied with the horizontal resolutions at 45-, 15-, and 5-km. The results revealed that, in comparison with ground observations, no single resolution can yield the best model performance for all variables across all stations. From a regional average perspective (i.e., across all monitoring sites), air temperature modeling was not sensitive to the grid resolution but wind and precipitation simulation showed the opposite. NU-WRF with the 5-km grid simulated the wind speed best, while the 45-km grid yielded the most realistic precipitation as compared to the site observations. For air quality simulations, finer resolution generally led to better comparisons with observations for O₃, CO, NO_x, and PM_{2.5}. However, the improvement of model performance on air quality was not linear with the resolution increase. The accuracy of modeled surface O₃ out of the 15-km grid was greatly improved over the one from the 45-km grid. Further increase of grid resolution to 5-km, however, showed diminished impact on model performance improvement on O₃ prediction. In addition, 5-km resolution grid showed large advantage to better capture the frequency of high pollution occurrences. This was important for assessment of noncompliance of ambient air quality standards, which was key to air quality planning and management. Balancing the modeling accuracy and resource limitation, a 15-km grid resolution was suggested for future MICS-Asia air quality modeling activity if the research region remained unchanged. This investigation also found out large overestimate of ground-level O₃ and underestimate of surface NO_x and CO, likely due to missing emissions of NO_x and CO.

28 1. Introduction

29 Air pollution is a threat to human health/climate and detrimental to ecosystem (Anenberg
30 et al., 2010; <https://www.who.int/airpollution/ambient/en/>). Lelieveld et al. (2015) estimated that
31 over 3 million premature mortality could be attributable to outdoor air pollution worldwide in 2010
32 based on their analysis of data and the results from a high-resolution global air quality model.
33 Since the turn of the 21st century, East Asia has undergone remarkable changes in air quality as
34 observed by satellite and ground stations (Jin et al., 2016; Krotkov et al., 2016). In the past decade,
35 haze (fine particle) pollution has become a household name in China and many severe haze events
36 have been reported and their formation mechanisms and associations with global- and meso-scale
37 meteorology have been analyzed (Zhao et al., 2013; Huang et al., 2014; Gao et al., 2016; Cai et
38 al., 2017; Zou et al., 2017). Meanwhile, ground level ozone has been a major air quality concern
39 in China (Wang et al., 2017; Lu et al., 2018), Japan (Akimoto et al., 2015), and South Korea (Seo
40 et al., 2014). In combination with observations from various platforms, chemical transport model
41 (CTM) remains an important tool to understand mechanisms, to investigate spatial-temporal
42 distributions, and to design feasible control strategies of air pollution. However, CTM model
43 uncertainties persist (e.g., Carmichael et al., 2008) and the interpretation of any model results needs
44 caution and exertion of careful analysis.

45 Inter-model comparison study provides a valuable way to understand model uncertainties
46 and sheds light on model improvements. With this as one of its major goals, the Model Inter-
47 Comparison Study for Asia (MICS-Asia) was initiated in 1998. Since then MICS-Asia has gone
48 through three phases with emphasis on various aspects of air pollution. Phase I focused on long-
49 range transport and deposition of sulfur over East Asia (Carmichael et al., 2002). Phase II expanded
50 the analysis on more pollutants including nitrogen compounds, particulate matter, and ozone, in
51 addition to sulfur (Carmichael et al., 2008). Fast moving to Phase III, MICS-Asia concentrated on
52 three topics with number one aiming at identifying strengths and weaknesses of current air quality
53 models to provide insights on reducing uncertainties (Gao et al., 2018). There are totally 14 CTMs
54 – 13 regional and 1 global – participating in the coordinated model experiment, which simulated
55 air quality over Asia throughout the year 2010. Due to the constrain of computing resources among
56 participating modeling groups, a 45-km horizontal resolution has been commanded for every team
57 to run the year-long experiment.

58 This relatively coarse spatial resolution raises the question of how representative the model
59 can resolve key issues relevant to air quality and its planning/regulation, e.g., heterogeneous
60 emissions, inhomogeneous land cover and meteorology. For example, Valari and Menut (2008)
61 explored the issue using the CHIMERE chemistry-transport model at various horizontal
62 resolutions over Paris. They found out that the ozone simulation was especially sensitive to the
63 resolution of emissions. However, the benefit of increasing emissions resolutions to improve ozone
64 forecast skills was not monotonic and at certain point the forecast accuracy decreased upon further
65 resolution increase. Using the Weather Research and Forecasting Chemistry model (WRF-Chem)
66 with various horizontal resolution (3 ~ 24 km) over the Mexico City, Tie et al. (2010) concluded
67 that a 1 to 6 ratio of grid resolution to city size appeared to be a threshold to improve ozone
68 forecasting skill over mega-city areas: the forecast would be improved significantly when model
69 resolution was below this threshold value. On contrary to Valari and Menut (2008), Tie et al. (2010)
70 suggested that the meteorology changes associated with the grid size choice played a more
71 prominent role in contributing to the improvement of ozone forecast skills. More recently, Neal et
72 al. (2017) employed a high-resolution (12 km) air quality model with high-resolution emissions
73 within the Met Office's Unified Model (AQUM) for air quality forecast over the Great Britain.

74 They found out that AQUM significantly improved the forecast accuracy of primary pollutants
75 (e.g., NO₂ and SO₂) but less obviously for secondary pollutants like ozone, as compared with a
76 regional composition-climate model (RCCM, 50 km horizontal resolution). But there was a
77 drawback from their conclusion in that the chemical mechanisms and photolysis rates utilized in
78 AQUM and RCCM were different, complicating the underlying reasons for changes in forecast
79 skills. Lee et al. (2018) examined the importance of aerosol-cloud-radiation interactions to
80 precipitation and the model resolution impact of key meteorological processes that affected
81 precipitation using the Advanced Research WRF model. They found that the coarse model
82 resolution would lower updraft, alter cloud properties (e.g, mass, condensation, evaporation, and
83 deposition), and reduce cloud sensitivity to ambient aerosol changes. They further concluded that
84 the uncertainty associated with resolution was much more than that related to cloud microphysics
85 parameterization. The resultant meteorological condition change would trigger air quality response
86 as well.

87 Despite the progress, the exploration of impacts of model resolution on local air quality
88 over Asia is rare. Taking advantage of the MICS-Asia platform, we examined the issue over the
89 MICS-Asia domain using the NASA Unified WRF (NU-WRF, Tao et al., 2013, 2016, 2018;
90 Peters-Lidard et al., 2015), focusing on the North China Plain (NCP) that was plagued by frequent
91 heavy air pollution episodes. The investigation would not only assist in gaining insights on how
92 model horizontal resolution affects simulated meteorology and air quality, but also contribute to
93 formulation of uncertainties resulted from model resolutions to the MICS-Asia community. The
94 latter would especially be valuable since most MICS-Asia Phase III model simulations were
95 conducted at a specific horizontal resolution (i.e., 45-km for most participants).

96

97 **2. NU-WRF model and experiment design**

98 NU-WRF is an integrated regional Earth-system modeling system developed from the
99 advanced research version of WRF-Chem (Grell et al., 2005), which represents atmospheric
100 chemistry, aerosol, cloud, precipitation, and land processes at convection-permitting spatial scales
101 (typically 1-6 km). NU-WRF couples the community WRF-Chem with NASA's Land Information
102 System (LIS), a software framework including a suite of land surface models (LSMs) that are
103 driven by satellite/ground observations and reanalysis data (Kumar et al., 2006; Peters-Lidard et
104 al., 2007). It also couples the Goddard Chemistry Aerosol Radiation and Transport (GOCART)
105 bulk aerosol scheme (Chin et al., 2002, 2007) with the Goddard radiation (Chou and Suarez, 1999)
106 and microphysics schemes (Tao et al., 2011; Shi et al., 2014) that allows for fully coupled aerosol-
107 cloud-radiation interaction simulations. In addition, NU-WRF links to the Goddard Satellite Data
108 Simulator Unit (G-SDSU), which converts simulated atmospheric profiles, e.g, clouds,
109 precipitation, and aerosols, into radiance or backscatter signals that can directly be compared with
110 satellite level-1 measurements at a relevant spatial and temporal scale (Matsui et al., 2009, 2013,
111 2014). In this study, NU-WRF has been employed to carry out the model simulations at various
112 horizontal resolutions using the same set of physical and chemical configurations.

113 A nested domain setup was configured to this investigation as shown Figure 1. The 45-km
114 resolution mother domain (d01) covered the MICS-Asia Phase III study region. The nested 15-km
115 (d02) and 5-km (d03) domains covered the East Asia and NCP, respectively. A one-way nesting
116 approach was applied so that the values of the mother domains were independent on those of the
117 respective nested domains. This analysis focused on NCP and its adjacent areas with over 1.1
118 million square kilometers. The key NU-WRF configurations included the updated Goddard
119 cumulus ensemble microphysics scheme (Tao et al., 2011), new Goddard long/shortwave radiation

120 scheme (Chou and Soares, 1999), Monin-Obukhov surface layer scheme, unified Noah land
 121 surface model (Ek et al., 2003) with LIS initialization (Peters-Lidard et al., 2015), Yonsei
 122 University planetary boundary layer scheme (YSU, Hong et al., 2006), new Grell cumulus scheme
 123 developed from the ensemble cumulus scheme (Grell and Devenyi, 2002) that allowed subsidence
 124 spreading (Lin et al., 2010), 2nd generation regional acid deposition model (RADM2, Stockwell et
 125 al., 1990; Gross and Stockwell, 2003) for trace gases and GOCART for aerosols. In this
 126 investigation, the option of fully coupled GOCART-Goddard microphysics and radiation schemes
 127 (Shi et al., 2014) was implemented to account for the aerosol-cloud-radiation interactions.

128 Anthropogenic emissions were from the mosaic Asian anthropogenic emissions inventory
 129 (MIX, Li et al., 2017) that was developed for the MICS-Asia Phase III. The MIX inventory was at
 130 the 0.25° by 0.25° resolution and projected to the study domain under the 45-, 15-, and 5-km
 131 horizontal resolutions. Fire emissions were from the 0.5° by 0.5° Global Fire Emissions Database
 132 version 3 (GFEDv3, van der Werf et al., 2010; Mu et al., 2011) and also projected to the targeted
 133 region. Biogenic emissions were computed online using the Model of Emissions of Gases and
 134 Aerosols from Nature version 2 (MEGAN2, Guenther et al., 2006). Dust and sea salt emissions
 135 were also calculated online using the dynamic GOCART dust emissions scheme (Kim et al, 2017)
 136 and sea salt scheme (Gong, 2003), respectively.

137 The meteorological Lateral Boundary Conditions (LBCs) were derived from the Modern
 138 Era Retrospective-Analysis for Research and Applications (MERRA, Rienecker et al., 2011). The
 139 trace gas LBCs were based on the 6-hour results from the Model for OZone And Related chemical
 140 Tracers (MOZART, Emmons et al., 2010). The aerosol LBCs were from the global GOCART
 141 simulation with a resolution of 1.25 (longitude) by 1 (latitude) degree (Chin et al., 2007). Three
 142 horizontal resolutions varied from 45-km to 5-km with 15-km in between. Terrain-following sixty
 143 vertical levels stretched from surface to 20 hPa with the 1st layer height of approximately 40 meters
 144 from surface. The simulation started on December 20, 2009, and ended on December 31, 2010,
 145 with the first 11 days as the spin-up.

146

147 3. Results

148 3.1. Comparisons with observations

149 The NU-WRF results out of different horizontal resolutions have compared with ground
 150 observations using the following statistic measures:

151	Correlation coefficient:	$r = \frac{\sum_{i=1}^n (m_i - \bar{m})(o_i - \bar{o})}{\sqrt{\sum_{i=1}^n (m_i - \bar{m})^2} \sqrt{\sum_{i=1}^n (o_i - \bar{o})^2}}$
152	Mean bias:	$MB = \frac{1}{n} \sum_{i=1}^n (m_i - o_i)$
153	Normalized mean bias:	$NMB = \frac{\sum_{i=1}^n (m_i - o_i)}{\sum_{i=1}^n o_i} \times 100\%$
154	Root mean square error:	$RMSE = \sqrt{\frac{\sum_{i=1}^n (m_i - o_i)^2}{n}}$
155	Normalized standard deviation:	$NSD = \frac{\sqrt{\frac{\sum_{i=1}^n (m_i - \bar{m})^2}{n-1}}}{\sqrt{\frac{\sum_{i=1}^n (o_i - \bar{o})^2}{n-1}}}$

156 Where, m_i and o_i denote for the modeled and observed values at time-space pair i ; \bar{m} and \bar{o}
 157 represent the average modeled and observed values, respectively. r describes the strength and
 158 direction of a linear relationship between two variables – a perfect correlation has a value of 1.
 159 NMB and MB depict the mean deviation of modeled results from the respective observations. A

160 perfect model simulation yields an *NMB* and a *MB* of 0. *RMSE* measures the absolute accuracy of
161 a model prediction. The smaller the *RMSE*, the better the model performance is. Similar to *NMB*
162 and *MB*, a *RMSE* of 0 indicates a perfect model prediction. *NSD* is a measure to check how well
163 the model can reproduce the variations of observations – a value of 1 represents a perfect
164 reproduction of observed variations.

165

166 3.1.1. Meteorology

167 The 2010 meteorological observations were collected at the standard stations operated by
168 China Meteorological Administration (CMA, <http://data.cma.cn/en>). The locations of each site
169 within our study domain were represented with the black dots in Figure 1. In total there were 77
170 sites reporting daily average values of wind speed (Wind), air temperature (Temp), and relative
171 humidity (RH), as well as daily total precipitation (Precip). Figure 2 (top row) shows the Taylor
172 diagram summarizing *r*, *NMB*, and *NSD* of the comparison of regional mean (average of
173 observations from 77 sites) daily meteorological variables. Along the azimuthal angle is *r*. *NSD*
174 is proportional to the radial distance from the origin. *NMB* (sign and range) are represented by the
175 geometric shapes. The statistical measures under 45-, 15-, and 5-km resolutions are represented by
176 color blue, green, and red, respectively. The closer to the point “Obs” on the Taylor diagram and
177 smaller of *NMB*, the better the model performance is.

178 It can be seen that the model horizontal resolution has little impact on surface air
179 temperature simulation. Regardless of resolution selections, the modeled temperature correlated
180 very well with the corresponding observations with *r* values all approaching 0.99. NU-WRF also
181 reproduced the observed temperature variations well with *NSD* ranging between 1.05 and 1.10.
182 Meanwhile, *NMB* was within $\pm 1\%$ for all experimented resolutions. *RMSEs* were 1.13 K, 2.26 K,
183 and 2.02 K for the 45-km, 15-km, and 5-km grids, respectively. The insensitivity of surface air
184 temperature to the choice of model resolutions was also reported by Gao et al. (2017), who used
185 WRF to explore the issue for summer seasons at the 36-, 12-, and 4-km resolutions.

186 On the other hand, the horizontal resolution has a remarkable effect on surface wind speed
187 as shown in Figure 2 (top row). At the 5-km resolution, NU-WRF yielded a *r* value of 0.75, *NMB*
188 of approximately 54%, and *NSD* of 1.78. NU-WRF simulated a large variation in wind than the
189 observed ones. As comparisons, the values of *r*, *NMB*, and *NSD* for 15-km and 45-km were 0.54,
190 95%, 2.14, and 0.71, 103%, 2.01, respectively. The respective *RMSEs* out of the 45-km, 15-km,
191 and 5-km grids were 2.87, 2.82, and 1.67 m s⁻¹. It was apparent that 5-km resolution gave the
192 overall best wind speed simulation compared to the observations, though NU-WRF overestimated
193 the surface wind speed in all cases. The wind speed overestimate, especially under low wind
194 conditions, was a common problem in all MICS-Asia participating models and other weather
195 forecast models (Gao et al., 2018). This overestimate stemmed from many factors, including but
196 not limited to terrain data uncertainty, poor representation of urban surface effect, horizontal and
197 vertical grid resolutions, etc. Dr. Yu (2014) in her doctoral dissertation pointed out that surface
198 wind simulation would be improved upon using more accurate land-use data. This is expected
199 since surface wind is largely dependent on the land surface characteristics, such as albedo and
200 roughness. High-resolution grid tends to have more accurate land-use representation seeing the
201 inhomogeneous nature of land type.

202 NU-WRF simulations at all three resolutions yielded the similar reproductions of the
203 observed variations in relative humidity (RH) with the *NSD* ranging between 0.87 and 0.88. The
204 modeled RH was less variable than the observed one. While the modeled RH at the 45-km
205 resolution (*r* = 0.84) better correlated with the observations than those at the finer resolutions did

206 (approximately 0.67 for both 15-km and 5-km resolutions), the *NMB* at this resolution was the
207 largest (-17%) among the three cases. The *NMBs* for 15-km and 5-km cases were -10% and -12%,
208 respectively. Overall, NU-WRF underestimated the surface RH. The respective *RMSEs* for 45-km,
209 15-km, and 5-km resolutions were 13.2%, 12.6%, and 13.3%. The simulation with the 15-km grid
210 appeared to yield the overall best RH in three cases.

211 It was interesting to find that NU-WRF simulated the precipitation best, as directly
212 compared to the rain gauge data, when using the 45-km grid. At this resolution, NU-WRF gave *r*
213 of 0.81, *NMB* of 1.7%, *RMSE* of 3.2 mm day⁻¹, and *NSD* of 1.41. As comparisons, the values of *r*,
214 *NMB*, *RMSE*, and *NSD* for 15-km and 5-km were 0.53, 76%, 5.7 mm day⁻¹, 1.71, and 0.52, 80%,
215 5.8 mm day⁻¹, 1.72, respectively. Finer resolutions indeed yielded worse results in precipitation
216 modeling as compared to the site data. This may be because precipitation was a very heterogeneous
217 phenomenon – finer model grid had larger chances to miss a precipitation event or hit an event
218 that was not existent, leading to a greater overall bias and a poorer correlation. On the contrary,
219 Gao et al. (2017) compared their WRF modeled results to the gridded precipitation based on the
220 daily rain gauge data that were gridded to the 0.125° resolution using the synergraphic mapping
221 algorithm with topographic adjustment to the monthly precipitation climatology (Maurer et al.,
222 2004). They reported that the modeled precipitation out of the 4-km resolution was much improved
223 over that out of the coarser 36- or 12-km resolutions.

224 The time series of daily mean wind speed, air temperature, and RH, as well as daily total
225 precipitation averaged over the monitoring sites is illustrated in Figure 1s in the supplement
226 material. It echoed the above findings based on the Taylor diagram. It appeared that NU-WRF
227 constantly overestimated surface wind speed throughout the year with large overestimate occurring
228 in fall and winter, while it severely underestimated RH in summer. Uncertainty in representation
229 of land surface characteristics at least partially explained these biases (Yu, 2014; Gao et al., 2018).
230 High-resolution grid tended to reduce the uncertainty in land surface representation, which would
231 be helpful to improving model performance in meteorology simulation. A more detailed
232 exploration of model-observation mismatch was insightful but beyond the scope of this research.

233

234 **3.1.2. Air quality**

235 The difference seen in the aforementioned meteorology would cause varied performances
236 on air quality simulations at various model horizontal resolutions. In this study, the NU-WRF
237 simulated surface air quality was compared to the corresponding observations. The 2010 ground-
238 level air quality data were obtained from the Chinese Ecosystem Research Network (CERN,
239 <http://www.cern.ac.cn>) operated by the Institute of Atmospheric Physics of Chinese Academy of
240 Sciences. There were 25 monitoring sites distributed within a 500 km by 500 km area centering
241 around Beijing, China (open diamond in Figure 1). The site locations and characteristics were
242 listed in Table 1. 22 out of 25 sites were either in an urban or a suburban setting, with the balance
243 being in a rural setting. Each site reported hourly concentrations of at least one of the following
244 six pollutants – ozone (O₃), nitrogen oxides (NO_x), carbon monoxide (CO), sulfur dioxide (SO₂),
245 and particulate matters with aerodynamic diameters less than 2.5 and 10 μm (PM_{2.5} and PM₁₀).

246

247 **a. Regional average**

248 First, the regional mean (averaged across 25 sites) daily surface concentrations from both
249 observations and simulations, paired in space and time, were calculated. The *r*, *NMB*, and *NSD*
250 were then computed and illustrated in a Taylor diagram (Figure 2 (bottom row)).

251 The six pollutants can be put into two groups – one most relevant to ozone photochemistry
252 including O₃, NO_x, and CO, and the other closely tied to aerosols including SO₂, PM_{2.5}, and
253 PM₁₀. It was readily seen that the *r* values of O₃, NO_x, and CO were not very sensitive to the
254 choice of model horizontal resolutions. For O₃, the *r* values for 45-km, 15-km, and 5-km grids
255 were all around 0.85. The respective *r* values were 0.84, 0.81, 0.80 for NO_x, and 0.80, 0.75, 0.73
256 for CO. In general, however, NU-WRF reproduced the observed variations in O₃, NO_x, and CO
257 better with a fine resolution than with a coarse one. *NSD* of 1.23 for O₃ at 5-km resolution was the
258 closest to 1 among three resolutions (1.24 for 15-km and 2.01 for 45-km). *NSDs* were 0.40, 0.36,
259 0.46 for NO_x, and 0.24, 0.27, 0.31 for CO, under the 45-km, 15-km, and 5-km resolutions,
260 respectively, suggesting that simulations with the finest resolution tended to reproduce the
261 observed variations better than the ones with coarse resolutions for these three trace gases.
262 Meanwhile, NU-WRF yielded the smallest bias when employing the fine resolution grid. *NMBs*
263 for O₃ decreased from 115% to 92% when grid resolutions increased from 45-km to 5-km. *NMBs*
264 were -38%, -30%, -18% for NO_x, and -61%, -55%, -51% for CO, under the 45-km, 15-km, and 5-
265 km resolutions, respectively. It was apparent that NU-WRF overestimated surface O₃ but
266 underestimated NO_x and CO, consistent with the findings in the companion MICS-Asia III studies
267 that based their results on ensemble model simulations (Li et al., 2019; Kong et al., 2019). The
268 majority of the air quality monitoring sites used in this study were in an urban setting, which
269 typically were in a VOC-limited regime. This meant that the underestimate of NO_x would reduce
270 the titration that consumed surface O₃ leading to its overestimate. We further analyzed the model
271 bias for daytime (8-18 local standard time) vs. nighttime. It was found that the nighttime biases for
272 surface O₃ and NO_x were approximately 2~4 times higher than those of daytime, consistent with
273 the finding that insufficient NO_x titration caused overestimate of modeled surface O₃.

274 NU-WRF simulated less variations in 3 aerosol related pollutants than those of
275 observations under all applied horizontal resolutions. The *NSDs* ranged from 0.56 (for SO₂ at 15-
276 km resolution) to 0.96 (for PM_{2.5} at 45-km resolution). Though it reproduced the observed SO₂
277 variations the best (*NSD* = 0.68) with the 5-km resolution, NU-WRF yielded the best *NSD* for
278 PM_{2.5} (0.96) and PM₁₀ (0.92) when the 45-km resolution was employed. Similar to 3 trace gases
279 relevant to surface O₃ formation, the choice of model resolution had a limited effect on *r* statistics.
280 The *r* values varied from 0.70 (45-km resolution) to 0.76 (both 15- and 5-km) for surface SO₂, and
281 from 0.68 (45-km resolution) to 0.63 (5-km) for PM_{2.5}. The *r* values for PM₁₀ were all around
282 0.58 under the selected resolutions. The impact of model resolution on *NMBs* showed mixed
283 information – while the smallest *NMBs* for SO₂ (20%) and PM₁₀ (-19%) were achieved using the
284 45-km resolution, the smallest *NMB* for PM_{2.5} (1.5%) was observed at the 15-km resolution. The
285 model underestimate of PM₁₀ was consistent with the findings of the companion investigation
286 using the multi-model ensemble analysis (Chen et al., 2019).

287 Figure 2s in the supplement material shows the time series of daily mean air quality
288 averaged over the monitoring sites for the year 2010. The constant underestimate of CO throughout
289 the year, severe underestimate of NO_x in fall and winter, and large underestimate of SO₂ in summer
290 all pointed out that the emissions inventory may be incomplete, agreeing with the reports by Kong
291 et al. (2019) and Li et al. (2019). In the future, improvement of the emissions inventory accuracy
292 and more realistic temporal emissions distribution may help improving NU-WRF performance in
293 simulating O₃ photochemistry.

294
295 ***b. Individual site***

296 The daily average concentrations of each pollutants were calculated and paired in space
297 and time at each air quality monitoring site. Then the statistics at each individual site was computed.
298 Figure 3 illustrates the comparisons of *MB*, *RMSE*, and correlation coefficient (*r*) of surface O₃
299 from different horizontal resolutions at each site. It can be found that there was no single resolution
300 that yielded the best correlation across all sites. For example, the simulation with the 45-km
301 horizontal resolution gave the best correlation over sites BD, CFD, CZ, HJ, SJZ, SQL, TG, TJ, TS,
302 XH, XL, YF, YJ, and ZJK. On the other end of spectrum, BJT, DT, and LTH achieved the best
303 correlation when the 5-km grid was applied. QHD saw the best correlation out of the simulation
304 with the 15-km resolution. In any cases, however, the variations of *r* values from different
305 horizontal resolutions at each site were small (less than 0.04). On the other hand, NU-WRF yielded
306 the worst *MB* and *RMSE* when employing the 45-km resolution grid, while *MB* and *RMSE* were
307 similar between simulations with 15-km and 5-km resolutions. Typically, at sites with
308 urban/suburban settings, *MB* (*RMSE*) based on the 45-km grid was approximately 15~30%
309 (20~40%) higher than that out of the 15-km or 5-km grids. It appeared that NU-WRF tended to
310 have a better performance on ground-level O₃ simulation when increasing the horizontal resolution
311 from 45-km to 15-km, but further finer resolution had diminished impact on improving surface O₃
312 modeling. This was consistent with the finding by Valari and Menut (2008) who concluded that
313 the benefit of finer horizontal resolution grid to improving surface O₃ forecast skill would diminish
314 at certain point.

315 Figure 4 shows the PM_{2.5} case of comparisons of *MB*, *RMSE*, and *r*. Only 10 sites reported
316 PM_{2.5} measurements over year 2010. In general, the NU-WRF simulation with the 45-km grid
317 correlated better to the respective observations than the other 2 resolutions. The only exception
318 was site BD that saw the best correlation for the 5-km resolution. *MB* and *RMSE* results were
319 mixed with no single resolution giving superior results across all sites. Over 2 rural sites (LS and
320 XL), the simulations with the 15-km or 5-km grids yielded remarkably smaller *MB* but correlated
321 less to the corresponding observations than the one with the 45-km grid. Over 8 urban/suburban
322 sites, BD, SQL, and TG experienced the smallest *MB* when employing the 5-km resolution grid,
323 while TG, TJ, and XH saw the least bias at the 45-km resolution. The smallest *MB* at BJT and
324 LTH occurred using the 15-km grid.

325 At the individual site level, the impact of grid resolution on surface NO_x and CO (figures
326 not shown) modeling was similar to that at the regional average. Finer resolution simulation
327 generally reduced *MB* and *RMSE*. The results out of the 45-km grid always had the largest bias.
328 The underestimates of NO_x at least partially explained the overestimate of surface O₃ at each site
329 due to a less efficient NO-titration of O₃. This suggested that a higher resolution modeling with
330 more accurate spatial representation of NO_x emissions would help improving its performance on
331 surface O₃ simulations.

332 The signals for SO₂ and PM₁₀ (figures not shown) simulations were mixed as well. For
333 example, the largest bias for SO₂ simulation over sites BD, CZ, GA, HS, LS, QA, QHD, XH, XL,
334 YF, and YJ occurred when applying the 45-km grid, while the maximum bias over BJT, DT, HJ,
335 LF, LTH, SJZ, SQL, TG, TJ, TS, ZJK, and ZZ happened at the 5-km resolution. Sites CD and
336 CFD saw the largest bias at the 15-km resolution. Unlike PM₁₀ that was almost always
337 underestimated at each site regardless of grid resolutions, SO₂ was overestimated at 18 out of 25
338 sites and underestimated at the remaining 7 sites.

339 An effort has been put to identify the potential reasons that caused the model-observation
340 discrepancy. First and as discussed previously, the spatial distribution of emissions was one key
341 to determining air quality forecast accuracy. Figure 3s (in supplement) shows the typical time

342 evolutions of surface O₃ and NO_x over the rural (XL) and urban (QHD) sites. It can readily be
343 seen that NO_x was underestimated at the urban site but overestimated at the rural site. The coarser
344 the grid resolution, the severer the underestimates/overestimates were. This indicated that the 45-
345 km resolution tended to smooth out emissions to make urban (or emissions centers) less polluted
346 but rural more polluted. It in turn led to an overestimate of surface O₃ over the urban sites mainly
347 due to the reduced NO_x titration effect, especially at night when there was no photochemical O₃
348 formation. The statistics showed that the bias of the modeled daytime (7 am ~ 7 pm local time)
349 average surface O₃ was 30% ~ 90% smaller than that of the daily average in the urban sites, no
350 matter which grid resolution was applied. This suggested that in the future the high-resolution
351 emissions, especially proper representation of emission gradients, would be helpful in improving
352 air quality prediction. The effect of emissions gradients associated with the grid resolution would
353 be further discussed in the inter-model comparison section.

354 Next, the driving meteorology, especially wind, was important to accurately forecast air
355 quality over coastal areas that bore sharp thermal contrasts. QHD site locates approximately 5 km
356 from the ocean and is subject to sea breeze effects. The detailed analysis of meteorology and air
357 quality over QHD was conducted. The results indicated that the choice of grid resolution had large
358 impacts on model simulations at this coastal site. The selection of the 5-km grid reduced biases of
359 both surface temperature and wind speed. The biases of temperature reduced from 1.22 K (45-km)
360 to -0.42 K (15-km), and further down to -0.31 K when the 5-km grid was applied. The biases of
361 surface wind speed for the 45-km, 15-km, and 5-km grids were 3.72, 4.19, and 1.95 m s⁻¹,
362 respectively. The improvement of meteorology forecast helped reducing the biases of air quality
363 modeling. The biases of O₃/NO_x for the 45-km, 15-km, and 5-km resolution grids were 29.94/-
364 22.46 ppbv, 24.09/-20.29 ppbv, 23.97/-17.95 ppbv, respectively. The improvement using the 15-
365 km grid over the 45-km grid was remarkable but that using the 5-km grid over the 15-km grid was
366 marginal. The result emphasized the importance of high-resolution modeling to improvements of
367 air quality forecast skills, especially at coastal and complex terrain areas (e.g., QHD and XL).

368 369 *c. Extreme values*

370 High concentrations of air pollutants are of more concerns because of their adverse health
371 effects on both human beings and ecosystem. High pollutant concentrations also pose a greater
372 risk for non-compliance of the ambient air quality standards. Therefore, evaluations of impacts of
373 grid resolution on extreme concentrations of air pollutants are desirable.

374 Figure 5 displays the probability density function distributions of six pollutants based on
375 hourly surface concentrations across the monitoring sites. This analysis was focused on high
376 pollutant concentrations with the cutoff values for CO, O₃, NO_x, SO₂, PM_{2.5}, and PM₁₀ being
377 1.1 ppmv, 60 ppbv, 25 ppbv, 5.5 ppbv, 15 μg m⁻³, and 30 μg m⁻³, respectively. It appeared that
378 NU-WRF, regardless of the grid resolutions, failed to simulate surface CO with concentrations
379 more than 4 ppmv, likely due to the underestimate of CO emissions (Kong et al., 2019). The grid
380 resolution appeared to have limited impacts on surface PM₁₀ simulations when its concentrations
381 were more than 200 μg m⁻³. On the other hand, the grid resolution showed large impacts on NU-
382 WRF's capability in simulating high surface concentrations of O₃, NO_x, SO₂, and PM_{2.5}. For
383 surface O₃ with concentrations more than 100 ppbv, the NU-WRF results with the 5-km grid
384 appeared to better agree with the probability distribution of observations. For surface NO_x with
385 concentrations more than 70 ppbv, the NU-WRF results with the 5-km resolution grid better
386 mimicked the observed distribution. Modeling with the 5-km grid also yielded the best results of

387 distributions, in comparisons to the respective observations, of SO₂ with concentrations more than
388 45 ppbv, and of PM_{2.5} with concentrations greater than 120 µg m⁻³.

389 Table 2 lists the occurrences of violations of China's national ambient air quality standards
390 (NAAQS) for the six pollutants from both observations and simulations, in which columns "Class
391 1" and "Class 2" list the standards for rural and urban-suburban sites, respectively, and column
392 "Frequency" indicates the time integration of each NAAQS. It was apparent that NU-WRF failed
393 to report CO violations at any grid resolutions. No CO NAAQS violation was simulated but the
394 observation showed that surface CO exceeded the national standard by more than 1000 times. NU-
395 WRF underestimated the NAAQS exceedances of NO_x and SO₂. A higher-resolution grid
396 appeared to be able to catch more violations although the modeled results at the 5-km resolution
397 only captured 33% and 10% observed exceedances of NO_x and SO₂, respectively. NU-WRF
398 overestimated surface O₃ and PM_{2.5} when their concentrations were more than the corresponding
399 NAAQS. The fine grid resolution (i.e., 5-km) appeared to largely reduce the overestimation of
400 surface O₃ exceedances as compared to the 45-km grid but only marginally compared with the 15-
401 km grid. Compared to the observed occurrences of surface O₃ standard violation (3,684), the
402 simulated exceedances were 5.7, 1.8, and 1.7 times higher when employing the 45-km, 15-km, and
403 5-km resolution grid, respectively. The observations showed 1,343 occurrences of surface PM_{2.5}
404 exceedances, while the modeled exceedances were 377, 267, and 231 more for the 45-km, 15-km,
405 and 5-km grids, respectively. As for surface PM₁₀, the modeled exceedances were approximately
406 27%, 43%, and 41% less than the observed one for the 45-km, 15-km, and 5-km grids, respectively.

407

408 **3.2. Inter-resolution comparisons**

409 It is informative to compare the NU-WRF results out of different horizontal resolutions.
410 This, in addition to the discussion in section 3.1.2.b, can help understand the reasons why model
411 resolution matters.

412

413 **3.2.1. Emissions**

414 There were two types of emissions applied in this study. One was the prescribed emissions
415 out of the anthropogenic and wild fire sources, and the other was emissions computed online using
416 the real-time meteorology (or dynamic emissions) including emissions from biogenic sources, dust
417 sources, and sea spray. Amounts and temporal variations of dynamic emissions depended on
418 surrounding environmental conditions. For example, air temperature and solar radiation regulates
419 biogenic emissions (Guenther et al., 2006). Surface wind speed plays a major role in both dust
420 (Ginoux et al., 2001; Chin et al., 2002) and sea salt emissions (Gong, 2003).

421 For the prescribed emissions, the differences of domain total masses out of each grid were
422 small (less than 5%). However, the emission gradient around sources of a fine resolution grid
423 appeared to be sharper than that of a coarse resolution grid. This meant that a coarse grid tended
424 to distribute the prescribed emissions more evenly into the domain, while a fine grid tended to
425 produce more extreme concentrations of primary pollutants (emitted directly from a source) such
426 as NO_x and SO₂, as shown in Table 2.

427 Online calculated emissions, on the other hand, displayed large differences in both gradient
428 and total mass. Similar to the case of prescribed emissions, a fine resolution grid tended to give a
429 sharper gradient of dynamic emissions than a coarse resolution grid did, as highlighted in Figure
430 6 (1st row) that illustrated the biogenic isoprene emissions (mol km⁻² hr⁻¹) on a typical summer day.
431 It was apparent that much more details were simulated using a fine resolution grid - the flow of
432 Yellow River can even be seen on the 5-km resolution map that was otherwise invisible from the

433 coarser resolution maps. Meanwhile, the total masses of dynamic emissions showed large
434 difference out of different resolution grids as listed in Table 3. On an annual basis, the domain
435 total isoprene emissions were 740,562 tons when estimated using the 45-km grid, approximately
436 85% and 86% of those with the 15-km and 5-km grids, respectively. The total dust emissions out
437 of the 45-km grid were 2,431 tons, only 54% and 62% of those based on the respective 15-km and
438 5-km grids. The percentage contrasts for sea salt emissions were even larger with emissions out of
439 the 15-km and 5-km grids being 1.3 and 1.6 times more than those of the 45-km grid, respectively.
440 It should be noted that although they differed greatly between out of the 45-km and 15-km grids,
441 the dynamic emissions out of the 5-km grid were much closer to those out of the 15-km grid,
442 partially explaining why the impact of model resolution on surface air quality was less remarkable
443 by increasing the resolution from 15-km to 5-km than from 45-km to 15-km.

444 The spatial (gradient) and mass variations in emissions out of different resolution grids
445 would result in difference in air quality simulations.

446

447 **3.2.2. Meteorology**

448 It's been reported that simulated meteorology varies in response to selections of model grid
449 resolutions (e.g., Tie et al., 2010; Lee et al., 2018). Meteorology plays an important role in
450 regulating regional air quality – it affects emissions amount originating from biogenic, dust, and
451 sea sources; it impacts atmospheric chemical and photochemical transformation; and it directs air
452 flows and the associated transport of trace gases and aerosols. In this investigation, a few
453 meteorological parameters key to air pollutant generation and accumulation were analyzed,
454 including surface wind, air temperature, downward shortwave flux at surface (SWDOWN),
455 planetary boundary layer height (PBLH), and cloud water (liquid + ice) path (CWP). We focused
456 on months that were prone to deteriorated PM_{2.5} (January) and O₃ (July) air quality as shown in
457 Figure 6 and Table 3.

458 NU-WRF simulated a similar direction of surface wind in July 2010 over the eastern
459 portion of the domain (2nd row of Figure 6). In general, average wind speed was larger over Bohai
460 Sea and Yellow Sea than over the surrounding land areas with a dominating wind direction being
461 south and southeast. Based on the results from the 15-km and 5-km grids, the peak average wind
462 speeds over 4 m s⁻¹ were found in Bohai Bay blowing to Tianjin and Beijing. However, such a
463 peak was absent from the 45-km grid simulation. In the west portion of the domain, the wind
464 direction generally changed from southeast in the south to southwest in the north. Compared to the
465 more organized wind directions out of the 45-km grid, wind directions out of the 15- and 5-km
466 grids were more chaotic. Averaged over the domain, the January mean wind speed out of the 45-
467 km grid was 2.92 m s⁻¹, which were 7% and 16% larger than those of the 15-km and 5-km grids,
468 respectively. The largest July mean wind speed was again simulated with the 45-km grid, 10% and
469 12% larger than the corresponding wind speed out of the 15-km and 5-km grids, respectively.

470 Overall, NU-WRF simulated very similar magnitudes and spatial patterns of surface air
471 temperature in July (3rd row of Figure 6), regardless of the selections of grid resolutions. Large
472 portions of the NCP experienced more than 300 K of July average air temperature. The minimum
473 average temperature of approximately 290 K was found in the central north part of the domain,
474 which was part of the Mongolian Plateau with the elevation being over 1,500 m above the sea level.
475 The domain average January and July surface air temperature were around 268 K and 300 K,
476 respectively, for simulations out of all three grids.

477 As expected, the modeling results from all three grids (4th row of Figure 6) showed that
478 July average PBLH over sea was much smaller than that over land. The large average PBLH (more

479 than 1,000 m) was found in the northwestern corner of the domain with a dominant land cover
480 type of grassland mosaiced with open shrubland that appeared to be drier than the other land cover
481 types in the domain. The high sensible heating associated with dry soil tended to produce the deep
482 PBL (Tao et al., 2013). The largest domain-average PBLHs in January and July were found from
483 the simulations out of the 15-km and 45-km grids, respectively. In January, the differences of the
484 domain-average PBLHs from different grid resolutions were small and within 2%. In July,
485 however, such difference can be over 9%.

486 Regardless of the grid resolutions, NU-WRF simulated a generally southeast-northwest
487 gradient of SWDOWN in July with the highest flux (over 300 W m^{-2}) occurring in the northwestern
488 domain (5th row of Figure 6). The differences between the maximum and minimum domain
489 average SWDOWN out of 3 grids were 5.6% and 3.3% in January and July, respectively.

490 CWP represented the vertical integration of cloud water (including both liquid and ice
491 phases) contents and can be regarded as a proxy of cloud amount and coverage. Opposite to the
492 SWDOWN case, NU-WRF modeled a generally northwest-southeast gradient of CWP in July with
493 the high values found in the southeastern domain (6th row of Figure 6). This is understandable
494 since cloud reflects and scatters the incoming solar radiation and thus affect SWDOWN. Large
495 cloud existence tended to reduce the solar flux reaching the underneath Earth surface. The CWP
496 differences among the model results out of different grid resolutions appeared to be larger than
497 SWDOWN differences. In July, the domain average CWPs out of the 15-km and 5-km grids were
498 37% and 33% larger than that of the 45-km grid, respectively. The gaps were even larger in January,
499 during which the domain average CWPs from the 15-km and 5-km grids were approximately 1.6
500 times larger than that from the 45-km grid.

501

502 **3.2.3. Air Quality**

503 In response to the aforementioned emissions and meteorological variations resulted from
504 the selections of model grid resolutions, changes in regional air quality ensued as illustrated in
505 Figure 7 and Table 3. This figure shows the July average concentrations of ground-level O_3 and
506 its precursors of NO_x and CO , as well as the January mean concentrations of surface SO_2 , $\text{PM}_{2.5}$,
507 and PM_{10} , during which month the respective pollutants tended to reach high concentrations.

508 O_3 is a secondary pollutant that is formed in the atmosphere through complex
509 photochemical processes upon existences of its precursors such as NO_x and volatile organic
510 compounds (VOC). Figure 7 (row 1) shows that the spatial distributions of surface O_3 are similar
511 to each other but the concentrations out of the 15-km and 5-km grids are smaller than those from
512 the 45-km grid. The domain average surface O_3 concentration in July was approximately 87 ppbv
513 based on the results from the 45-km grid, 26% and 25% higher than those out of the 15-km and 5-
514 km grid, respectively. In January, however, the highest domain average concentration occurred
515 when the 5-km grid was used, which was 5.3% higher than that out of the 45-km grid.

516 For the primary pollutants, i.e., NO_x , CO , and SO_2 (rows 2-4 of Figure 7, respectively),
517 which were emitted directly by their sources, the spatial distributions of their concentrations
518 mimicked closely with their emission distributions. High concentrations centered around emission
519 sources with a reducing gradient outward. The domain average concentrations of these 3 pollutants
520 out of the 45-km grid results were always the largest in both January and July. The average surface
521 NO_x concentrations from the simulations out of the 15-km and 5-km grids were around 24% lower
522 than their counterparts out of the 45-km grid in January. In July, the differences were reduced to
523 7.9% and 11.8% for the 15-km and 5-km grids, respectively. On the other hand, the larger
524 percentage differences, as compared to the results out of the 45-km grid, occurred in July than in

525 January for both CO and SO₂. For example, the surface CO concentrations out of the 5-km grid
526 were 12.3% and 30.6% lower than those based on the 45-km grid in January and July, respectively.
527 The respective ground-level SO₂ concentrations from the 5-km grid were 20.5% and 38.9% lower
528 than those from the 45-km grid in January and July.

529 It was interesting to note that among the 3 cases, the domain average July surface O₃ and
530 NO_x concentrations were both the highest out of the 45-km grid, contrary to the results discussed
531 in section 3.1.2a where the highest O₃ concentration occurred out of the simulation using the 45-
532 km grid while the highest NO_x concentration happened with the 5-km grid. This seemingly
533 contradicting result was internally consistent. Section 3.1.2a actually depicted the average surface
534 concentrations in an urban environment (23 of 25 monitoring sites were in an urban/suburban
535 setting), where surface O₃ formation was typically VOC controlled such that NO tended to
536 consume O₃ through titrations. As discussed in section 3.2.1, a 5-km grid gave a much sharper
537 emissions gradient with anthropogenic emissions concentrating in urban/suburban areas. This led
538 to higher NO_x concentrations around urban/suburban areas out of the simulation with the 5-km
539 grid, which effectively resulted in lower O₃ concentrations there through the NO titration effect.
540 The domain average discussed in this section, however, was the average covering the vast rural
541 area that generally was NO_x-limited such that surface O₃ formation was controlled by the
542 availability of NO_x – more NO_x resulting in more O₃ through photochemical processes. In this
543 case, the 45-km grid tended to distribute NO_x emissions more evenly in the region, effectively
544 decreasing the surface NO_x concentration in urban areas but increasing it over rural areas. The
545 larger average July wind speed simulated by the 45-km grid (Figure 6 and Table 3) further
546 smoothed out the NO_x distribution in NCP. This in turn increased the domain average surface O₃
547 concentration via photochemistry based on the 45-km resolution results. In addition, vertical lifting
548 played an important role in explaining the maximum regional O₃ in July simulated by the 45-km
549 grid as compared to the results by the other two grid resolutions. As displayed in Figure 4s in the
550 supplement material, a fine resolution modeling (e.g., 5-km) tended to produce a stronger updraft
551 than a coarse resolution modeling (e.g., 45-km), consistent with the findings by Lee et al. (2018).
552 The strong uplift would bring more surface pollutants such as NO_x into the upper atmosphere, thus
553 further reducing the NO_x availability at ground limiting the surface ozone production but
554 increasing its formation in the upper atmosphere.

555 Vertical distributions of O₃ also tend to have a sizable impact on next day's surface O₃
556 levels (e.g., Kuang et al., 2011; Caputi et al., 2019). Figure 8 illustrates the domain average profiles
557 of vertical wind, NO_x, O₃ (panels a~c), and the average diurnal distribution of surface O₃ (panel
558 d) over July. Here we limited our discussion on the results from the 15- and 5-km grids since the
559 45-km grid artificially allowed more NO_x emissions spreading to rural areas to produce much
560 more O₃ as shown in the previous paragraph. Lee et al. (2018) claimed that a coarse resolution
561 model appeared to lower updraft as compared with a fine resolution modeling. This study agreed
562 with their finding as illustrated in Figure 8 (panel a). The domain average July vertical wind out
563 of the simulation with the 5-km grid ranged from 0.25 to 0.45 cm s⁻¹ (upward) between 800 hPa
564 and 400 hPa, stronger than the corresponding one out of the 15-km grid. The reason was complex
565 and the aerosol-cloud interaction induced freezing/evaporation-related invigoration mechanism
566 played a role (Lee et al., 2018). The stronger upward wind tended to lift more gaseous pollutants
567 up to the free troposphere as shown in Figure 8 (panel b (NO_x) and c (O₃)). The pollutants there
568 would have visible impacts on the following-day surface air quality, especially on O₃ levels at
569 night and in the morning when sun breaks out the nocturnal planetary boundary layer, as evidenced
570 in Figure 8 (panel d). At night with no photochemical formation, surface O₃ concentration was

571 largely controlled by upper-level O₃ mixing down, NO titration and O₃ dry deposition. With the
572 virtually same average surface NO concentrations out of the 15- and 5-km grids, the upper-level
573 O₃ mixing down appeared to control the relative magnitudes of surface O₃ concentrations
574 simulated using the 15- and 5-km grids. This partially explained why, at night and early morning,
575 the ground level O₃ concentrations were higher out of the 5-km grid than from the 15-km grid.
576 During daytime when the photochemical formation of O₃ takes control, the regional average
577 surface O₃ concentrations is largely determined by the availability of O₃ precursors (i.e., NO_x and
578 VOC) and ambient environmental conditions. In this case, more spreading NO_x emissions out of
579 the 15-km grid appeared to generate more surface O₃ than the 5-km grid did.

580 PM_{2.5} and PM₁₀ were mixed pollutants that not only were emitted by various sources but
581 also were generated in the atmosphere through physical and chemical processes. Figure 7 shows
582 that high surface concentrations of PM_{2.5} (more than 120 µg m⁻³, row 5) and of PM₁₀ (more than
583 170 µg m⁻³, row 6) were still found around the source areas based on the modeling results out of
584 the 15-km and 5-km grids. However, high PM_{2.5} and PM₁₀ concentrations spread out to larger
585 areas based on the results from the 45-km grid as compared to the ones from the finer grid
586 resolutions. Similar to the primary pollutants, the largest domain average surface concentrations
587 occurred when a 45-km grid was used for the NU-WRF simulation. The domain average PM_{2.5}
588 concentrations out of the 15-km and 5-km grids in January were 15.7% and 14% lower than those
589 from the 45-km grid, respectively. The surface PM_{2.5} concentration differences among results out
590 of different grid resolutions grew larger in July, reaching 48% when comparing the result from the
591 5-km grid to that from the 45-km grid. The domain average surface PM₁₀ concentrations showed
592 similar pattern to that of PM_{2.5} with the results out of the 5-km grid being 12.2% (January) and
593 44.2% (July) smaller than that from the 45-km grid.

594 It is worth noting that the magnitudes and spatial distributions of ground-level pollutants
595 were close to each other between the results out of the 15-km and 5-km grids. This again indicates
596 that the improvement of fine grid resolution modeling reduces at a certain point. In future MICS-
597 Asia efforts, a 15-km grid appears to offer the optimized results balanced with performance and
598 resources.

599 600 **4. Summary**

601 Contributing to MICS-Asia Phase III whose goals included identifying and reducing air
602 quality modeling uncertainty over the region, this investigation examined the impact of model grid
603 resolutions on the performances of meteorology and air quality simulation. To achieve this, NU-
604 WRF was employed to simulate 2010 air quality over the NCP region with three grid resolutions
605 of 45-km, 15-km, and 5-km. The modeling results were compared to the observations of surface
606 meteorology archived by CMA, and of ground-level air quality collected in CERN. The inter-
607 model comparison among the simulation results out of three grids were also conducted to
608 understand the reasons why model resolution mattered.

609 The analysis showed that there was no single resolution which would yield the best
610 reproduction of meteorology and air quality across all monitoring sites. From a regional average
611 prospective (i.e., across all monitoring sites in this study), the choice of grid resolution appeared
612 to have a minimum influence on air temperature modeling but affected wind, RH, and precipitation
613 simulation profoundly. A 5-km grid appeared to give the best wind simulation as compared to the
614 observations quantified by bias, RMSE, standard deviation, and correlation. Compared to the one
615 using the 45-km grid, the simulated wind speed from the 5-km grid reduced the positive bias by
616 46.8%. While a 15-km grid yielded the best overall performance on RH modeling, the result out

617 of the 45-km grid gave the most realistic reproduction of precipitation. The statement on
618 precipitation should be taken with caution since it was based on the comparison with the site
619 observations. Seeing the very heterogeneous nature of precipitation, the penalty of model hitting
620 or missing a rain event was severe. Thus, the coarse grid covering more areas within a grid cell
621 would reduce chances of mistaken precipitation hitting or missing simulations. However, a
622 comparison of modeled precipitations to gridded “observation” that was re-constructed using the
623 synergraphic mapping algorithm with topographic adjustment to the monthly precipitation
624 climatology showed opposite result, where the fine resolution modeling showed superior
625 reproduction of precipitation than the coarse resolution simulation (Gao et al., 2017).

626 The simulated meteorology differences due to the selection of grid resolution would
627 consequently lead to differences in air quality simulation. Air pollutant concentrations were
628 basically determined by their emissions and underlying meteorology that directed their formation
629 (e.g., O₃ and aerosols), transport, and removal processes. For the prescribed emissions originated
630 from anthropogenic and wild fire sources, the grid resolution had limited influence on emission
631 amount – less than 5% difference with each other under the different resolution grids – but large
632 impact on emission spatial distribution with sharper emission gradient around sources out of a fine
633 resolution grid than from a coarse resolution one. For the dynamic emissions driven by
634 meteorology, not only was an emission gradient around a source larger out of a higher resolution
635 grid, but also the total emission amount varied greatly. For example, the domain total annual
636 biogenic isoprene emissions from a 5-km grid was about 16% larger than those out of a 45-km
637 grid due to the underlying differences in land cover and meteorology.

638 Though the impact of grid resolution on air quality varied from location to location, finer
639 grid yielded better results for daily mean surface O₃, NO_x, CO, and PM_{2.5} simulations from a
640 regional average perspective. For example, after reducing the grid resolution from 45-km to 15-
641 km, the positive bias of daily mean surface O₃ and PM_{2.5} decreased by 15% and 75%, respectively.
642 Fine resolution modeling was especially beneficial to high pollutant concentration forecast. This
643 was important to air quality management. Taking China’s NAAQS as cutoff values for each
644 pollutant, the frequencies of noncompliance occurrences of O₃, NO_x, SO₂, and PM_{2.5} out of the
645 5-km grid simulation were much closer to the observations than those out of the 45-km modeling
646 were. For example, the simulation with the 5-km grid produced 168% and 17% more exceedances
647 in NAAQS of O₃ and PM_{2.5}, respectively, whereas the respective exceedances were 573% and
648 28% more with modeling using the 45-km grid, as compared to the observed exceedances. It also
649 was worth noting that the benefit of increasing grid resolution to better surface O₃ and PM_{2.5}
650 simulations started to diminish when the horizontal resolution reached 15-km, agreeing with the
651 finding by Valari and Menut (2008). There was a caveat, though. The anthropogenic MIX and fire
652 GFEDv3 emissions inventories bore the 0.25° by 0.25° and 0.5° by 0.5° resolution, respectively.
653 These resolutions cannot resolve the 5-km grid. Should a 5-km resolution emissions inventory be
654 available and used, the benefit of high-resolution modeling would likely be more prominent.

655 It should be pointed out that NU-WRF significantly overestimated surface O₃ concentration
656 but underestimated ground-level CO and NO_x concentrations regardless of grid resolutions. This
657 was true not only on the regional averages but also at majority of the monitoring sites. The missing
658 emissions was believed to be largely responsible for this result (Kong et al., 2019). Underestimate
659 of surface NO_x tended to increase ground-level O₃ due to the reduced titration effect, especially at
660 night over urban areas that were typically NO_x abundant.

661 In conclusion, grid resolution had a profound effect on NU-WRF performance on
662 meteorology and air quality over the East Asia. Fine resolution grid did not always generate the

663 best modeling results and the proper selection of horizontal resolution hinged on investigation
664 topics for a given set of physics and chemistry choices in a model. With regard to MICS-Asia
665 Phase III whose major goal was to examine regional air quality, in general, the finer the grid
666 resolution was, the better the simulation results would be. This was especially true over the coastal
667 areas and complex terrains where a sharp local energy gradient existed. Fine resolution grid was
668 also extremely helpful to reproducing pollutants at higher concentrations that were most relevant
669 to air quality planning and management. However, the benefit of high resolution was not linear
670 with the decrease of grid size. At certain point, the improved modeling accuracy due to an increase
671 in grid resolution was so marginal that it cannot justify the computational cost associated with the
672 fine grid simulation. Based on the balance of modeling accuracy and efficiency, a 15-km horizontal
673 grid appeared to be an appropriate choice to optimize model performance and resource usage if
674 the study domain remained unchanged for future MICS-Asia activities. The study suggested that
675 the high-resolution emissions, especially the proper representation of emission gradients, would
676 be helpful in improving air quality prediction. Moreover, the profile measurements of both
677 meteorology and air quality, in supplement with the ground monitoring networks, would be greatly
678 helpful to identifying model deficiencies and thus improving model forecast skills.

679

680 **Competing interests**

681 The authors declare that they have no conflict of interest.

682

683 **Author contribution**

684 ZT and MC designed the experiments. ZT, MG, TK, DK, and HB carried out the
685 experiments working on various modeling components. YW and ZL collected, organized, and
686 archived the ground air quality measurement data. All authors contributed to model result analysis
687 and interpretation. ZT prepared the manuscript with contributions from all co-authors.

688

689 **Acknowledgement**

690 This work was supported by the NASA's Atmospheric Composition: Modeling and
691 Analysis Program (ACMAP) and Modeling, Analysis, and Prediction (MAP) program. The
692 authors thank MICS-Asia for its organized platform of discussion and data sharing. This work is
693 not possible without the supercomputing and mass storage support by NASA Center for Climate
694 Simulation (NCCS). All data collected and generated for this research are archived and stored on
695 NCCS servers. Due to the sheer size of data, it is impractical to upload data to a public domain
696 repository. However, the authors will be happy to share data on an individual request basis.

697

698

699 **References**

- 700 Akimoto, H., Mori, Y., Sasaki, K., Nakanishi, H., Ohizumi, T., and Itano, Y.: Analysis of
 701 monitoring data of ground-level ozone in Japan for long-term trend during 1990-2010:
 702 Causes of temporal and spatial variation, *Atmos. Environ.*, 102, 302-310, 2015.
- 703 Anenberg, S. C., Horowitz, L. W., Tong, D. Q., and West J. J.: An estimate of the global burden
 704 of anthropogenic ozone and fine particulate matter on premature human mortality using
 705 atmospheric modeling, *Environ. Health Perspect.*, 118(9), 1189-1195,
 706 doi:10.1289/ehp.0901220, 2010.
- 707 Cai, W., Li, K., Liao, H., Wang, H., and Wu, L.: Weather conditions conducive to Beijing severe
 708 haze more frequent under climate change, *Nature Climate Change*, 7, 257-263,
 709 doi:10.1038/NCLIMAE3249, 2017.
- 710 Caputi, D. J., Faloon, I., Trousdell, J., Smoot, J., Falk, N., and Conley, S.: Residual layer ozone,
 711 mixing, and the nocturnal jet in California's San Joaquin Valley, *Atmos. Chem. Phys.*, 19,
 712 4721-4740, doi:10.5194/acp-19-4721-2019, 2019.
- 713 Carmichael, G., Calori, G., Hayami, H., Uno, I., Cho, S. Y., Engardt, M., Kim, S. B., Ichikawa,
 714 Y., Ikeda, Y., Woo, J. H., Ueda, H., and Amann, M.: The MICS-Asia study: model
 715 intercomparison of long-range transport and sulfur deposition in East Asia, *Atmos. Environ.*,
 716 36, 175-199, 10.1016/s1352-2310(01)00448-4, 2002.
- 717 Carmichael, G., Sakurai, T., Streets, D., Hozumi, Y., Ueda, H., Park, S., Fung, C., Han, Z., Kajino,
 718 M., and Engardt, M.: MICS-Asia II: The model intercomparison study for Asia Phase II:
 719 methodology and overview of findings, *Atmos. Environ.*, 42, 3468-3490,
 720 10.1016/j.atmosenv.2007.04.007, 2008.
- 721 Chen, L., Gao, Y., Zhang, M., Fu, J. S., Zhu, J., Liao, H., Li, J., Huang, K., Ge, B., Wang, X.,
 722 LAM, Y. F., Lin, C.-Y., Itahashi, S., Nagashima, T., Kajino, M., Yamaji, K., Wang, Z., and
 723 Kurokawa, J.-I.: MICS-Asia III: Multi-model comparison and evaluation of aerosol over East
 724 Asia, *Atmos. Chem. Phys. Discuss.*, <http://doi.org/10.5194/acp-2018-1346>, in review, 2019.
- 725 Chin, M., Ginoux, P., Kinne, S., Torres, O., Holben, B. N., Duncan, B. N., Martin, R. V., Logan,
 726 J. A., Higurashi, A., and Nakajima, T.: Tropospheric aerosol optical thickness from the
 727 GOCART model and comparisons with satellite and Sun photometer measurements, *J.*
 728 *Atmos. Sci.*, 59, 461-483, 2002.
- 729 Chin, M., Diehl, T., Ginoux, P., and Malm, W.: Intercontinental transport of pollution and dust
 730 aerosols: implications for regional air quality, *Atmos. Chem. Phys.*, 7, 5501-5517,
 731 doi:10.5194/acp-7-5501-2007, 2007.
- 732 Chou, M.-D. and Suarez, M. J.: A solar radiation parameterization (CLIRAD-SW) for atmospheric
 733 studies, NASA Tech. Rep. NASA/TM-1999-10460, vol. 15, 38 pp, 1999.
- 734 Ek, M. B., Mitchell, K. E., Lin, Y., Rogers, E., Grunmann, P., Koren, V., Gayno, G., and Tarpley,
 735 J. D.: Implementation of Noah land surface model advances in the National Centers for
 736 Environmental Prediction operational mesoscale Eta Model, *J. Geophys. Res.*, 108, 8851,
 737 doi:10.1029/2002JD003296, 2003.
- 738 Emmons, L. K., Walters, S., Hess, P. G., Lamarque, J.-F., Pfister, G. G., Fillmore, D., Granier, C.,
 739 Guenther, A., Kinnison, D., Laepple, T., Orlando, J., Tie, X., Tyndall, G., Wiedinmyer, C.,
 740 Baughcum, S. L., and Kloster, S.: Description and evaluation of the Model for Ozone and
 741 Related chemical Tracers, version 4 (MOZART-4), *Geosci. Model Dev.*, 3, 43-67, 2010.
- 742 Gao, M., Carmichael, G. R., Wang, Y., Saide, P. E., Yu, M., Xin, J., Liu, Z., and Wang, Z.:
 743 Modeling study of the 2010 regional haze event in the North China Plain, *Atmos. Chem.*
 744 *Phys.*, 16, 1673-1691, doi:10.5194/acp-16-1673-2016, 2016.

745 Gao, M., Han, Z., Liu, Z., Li, M., Xin, J., Tao, Z., et al.: Air quality and climate change, Topic 3
746 of the Model Inter-Comparison study for Asia Phase III (MICS-Asia III) – Part 1: Overview
747 and model evaluation, *Atmos. Chem. Phys.*, 18 (7), 4859-4884, doi:10.5194/acp-18-4859-
748 2018, 2018.

749 Gao, Y., Leung, L. R., Zhao, C., and Hagos, S.: Sensitivity of U.S. summer precipitation to model
750 resolution and convective parameterizations across gray zone resolution, *J. Geophys. Res.*
751 *Atmos.*, 122, 2,714-2,733, doi:10.1002/2016JD025896, 2017.

752 Ginoux, P., Chin, M., Tegen, I., Prospero, J., Holben, B., Dubovik, O., and Lin, S.-J.: Sources and
753 global distributions of dust aerosols simulated with the GOCART model, *J. Geophys. Res.*,
754 106, 20,255-20,273, 2001.

755 Gong, S. L.: A parameterization of sea-salt aerosol source function for sub- and super-micron
756 particles, *Glob. Biogeochemical Cycles*, 17, No. 4, 1097, doi: 10.1029/2003GB002079, 2003.

757 Grell, G. A. and Devenyi, D.: A generalized approach to parameterizing convection combining
758 ensemble and data assimilation techniques, *Geophys. Res. Lett.*, 29, 1693,
759 doi:10.1029/2002GL015311, 2002.

760 Grell, G. A., Peckham, S. E., Schmitz, R., McKeen, S. A., Frost, G., Skamarock W. C., and Eder,
761 B.: Fully coupled “online” chemistry within the WRF model, *Atmos. Environ.*, 39, 6957–
762 6975, 2005.

763 Gross, A. and Stockwell, W. R.: Comparison of the EMEP, RADM2 and RACM Mechanisms, *J.*
764 *Atmos. Chem.*, 44, 151-170, 2003.

765 Guenther, A, Karl, T., Harley, P., Wiedinmyer, C., Palmer, P. I., and Geron, C.: Estimates of global
766 terrestrial isoprene emissions using MEGAN (Model of Emissions of Gases and Aerosols from
767 Nature), *Atmos. Chem. Phys.*, 6, 3181-3210, 2006.

768 Hong, S. Y., Noh, Y., and Dudhia, J.: A new vertical diffusion package with an explicit treatment
769 of entrainment processes, *Mon. Wea. Rev.*, 134, 2318-2341, 2006.

770 Huang, R.-J., Zhang, Y., Bozzetti, C., Ho, K.-F., Cao, J.-J., Han, Y., Daellenbach, K. R., Slowik,
771 J. G., Platt, S. M., Canonaco, F., Zotter, P., Wolf, R., Pieber, S. M., Bruns, E. A., Crippa, M.,
772 Ciarelli, G., Piazzalunga, A., Schwikowski, M., Abbaszade, G., Schnelle-Kreis, J.,
773 Zimmermann, R., An, Z., Szidat, S., Baltensperger, U., Haddad, I. E., and Prevot, A. S. H.:
774 High secondary aerosol contribution to particulate pollution during haze events in China,
775 *Nature*, 514, 218-222, doi:10.1038/nature13774, 2014.

776 Jin, Y., Andersson, H., and Zhang, S.: Air pollution control policies in China: A retrospective and
777 prospects, *Int. J. Environ. Res. Public Health*, 13(12), 1219, doi:10.3390/ijerph13121219,
778 2016.

779 Kim, D., Chin, M., Kemp, E. M., Tao, Z., Peters-Lidard, C. D., and Ginoux, P.: Development of
780 high-resolution dynamic dust source function – A case study with a strong dust storm in a
781 regional model, *Atmos. Environ.*, 159, 11-25, doi:10.1016/j.atmosenv.2017.03.045, 2017.

782 Kong, L., Tang, X., Zhu, J., Wang, Z., Fu, J. S., Wang, X., Itahashi, S., Yamaji, K., Nagashima,
783 T., Lee, H.-J., Kim, C.-H., Lin, C.-Y., Chen, L., Zhang, M., Tao, Z., Li, J., Kajino, M., Liao,
784 H., Sudo, K., Wang, Y., Pan, Y., Tang, G., Li, M., Wu, Q., Ge, B., and Carmichael, G. R.:
785 Evaluation and uncertainty investigation of the NO₂, C and NH₃ modeling over China under
786 the framework of MICS-Asia III, *Atmos. Chem. Phys. Discuss.*, [http://doi.org/10.5194/acp-](http://doi.org/10.5194/acp-2018-1158)
787 [2018-1158](http://doi.org/10.5194/acp-2018-1158), accepted, 2019.

788 Krotkov, N. A., McLinden, C. A., Li, C., Lamsal, L. N., Celarier, E. A., Marchenko, S. V., Swartz,
789 W. H., Bucsela, E. J., Joiner, J., Duncan, B. N., Boersma, K. F., Veefkind, J. P., Levelt, P.
790 F., Fioletov, V. E., Dickerson, R. R., He, H., Lu, Z., and Streets, D. G.: Aura OMI

791 observations of regional SO₂ and NO₂ pollution changes from 2005 to 2015, *Atmos. Chem.*
792 *Phys.*, 16(7), 4605–4629, doi:10.5194/acp-16-4605-2016, 2016.

793 Kumar, S. V., Peters-Lidard, C. D., Tian, Y., Houser, P. R., Geiger, J. Olden, S., Lighty, L.,
794 Eastman, J. L., Doty, B., Dirmeyer P., Adams, J., Mitchell K., Wood, E. F., and Sheffield, J.:
795 Land Information System – An Interoperable Framework for High Resolution Land Surface
796 Modeling, *Environ. Modelling & Software*, 21, 1,402-1,415, 2006.

797 Kuang, S., Newchurch, M. J., Burris, J., Wang, L., Buckley, P. I., Johnson, S., Knupp, K., Huang,
798 G., Phillips, D., and Canrell, W.: Nocturnal ozone enhancement in the lower troposphere
799 observed by lidar, *Atmos. Environ.*, 45, 6078-6084, 2011.

800 Lee, S. S. Li, Z., Zhang, Y. Yoo, H., Kim, S., Kim, B.-G., Choi, Y.-S., Mok, J., Um, J., Choi, K.
801 O., and Dong, D.: Effects of model resolution and parameterizations on the simulations of
802 clouds, precipitation, and their interactions with aerosols, *Atmos. Chem. Phys.*, 18, 13–29,
803 doi:10.5194/acp-18-13-2018, 2018.

804 Lelieveld, J., Evans, J. S., Fnais, M., Giannadaki D., and Pozzer, A.: The contribution of outdoor
805 air pollution sources to premature mortality on a global scale, *Nature*, 525, 367-371, 2015.

806 Li, J., Nagashima, T., Kong, L., Ge., B., Yamaji, K., Fu, J. S., Wang, X., Fan, Q., Itahashi, S., Lee,
807 H.-J., Kim, C.-H., Lin, C.-Y., Zhang, M., Tao, Z., Kajino, M., Liao, H., Li, M., Woo, J.-H.,
808 Kurokawa, J., Wang, Z., Wu, Q., Akimoto, H., Carmichael, G. R., and Wang, Z.: Model
809 evaluation and intercomparison of surface-level ozone and relevant species in East Asia in the
810 context of MICS-Asia phase III, Part I: overview, *Atmos. Chem. Phys.*, 19, 12993-13015,
811 <http://doi.org/10.5194/acp-19-12993-2019>, 2019.

812 Li, M., Zhang, Q., Kurokawa, J. I., Woo, J. H., He, K., Lu, Z., Ohara, T., Song, Y., Streets, D. G.,
813 Carmichael, G. R., Cheng, Y., Hong, C., Huo, H., Jiang, X., Kang, S., Liu, F., Su, H., and
814 Zheng, B.: MIX: a mosaic Asian anthropogenic emission inventory under the international
815 collaboration framework of the MICS-Asia and HTAP, *Atmos. Chem. Phys.*, 17, 935-963,
816 doi:10.5194/acp-17-935-2017, 2017.

817 Lin, M., Holloway, T., Carmichael, G. R., and Fiore, A. M.: Quantifying pollution inflow and
818 outflow over East Asia in spring with regional and global models, *Atmos. Chem. Phys.*, 10,
819 4221-4239, doi: 10.5194/acp-10-4221-2010, 2010.

820 Lu, X., Hong, J., Zhang, L., Cooper, O. R., Schultz, M. G., Xu, X., Wang, T., Gao, M., Zhao, Y.,
821 and Zhang, Y.: Severe surface ozone pollution in China: A global perspective, *Environ. Sci.*
822 *Technol. Lett.*, 5, 487-494, 2018.

823 Matsui, T., Tao, W.-K., Masunaga, H., Kummerow, C. D., Olson, W. S., Teruyuki, N., Sekiguchi,
824 M., Chou, M., Nakajima, T. Y., Li, X., Chern, J., Shi, J. J., Zeng, X., Posselt, D. J., and
825 Suzuki, K.: Goddard Satellite Data Simulation Unit: Multi-Sensor Satellite Simulators to
826 Support Aerosol- Cloud-Precipitation Satellite Missions, *Eos Trans.*, 90(52), Fall Meet.
827 *Suppl.*, Abstract A21D-0268, 2009.

828 Matsui, T., Iguchi, T., Li, X., Han, M., Tao, W.-K., Petersen, W., L'Ecuyer, T., Meneghini, R.,
829 Olson, W., Kummerow, C. D., Hou, A. Y., Schwaller, M. R., Stocker, E. F., and Kwiatkowski,
830 J.: GPM satellite simulator over ground validation sites, *Bull. Am. Meteor. Soc.*, 94, 1653-
831 1660, doi:10.1175/BAMS-D-12-00160.1, 2013.

832 Matui, T., Santanello, J., Shi, J. J., Tao, W.-K., Wu, D., Peters-Lidard, C., Kemp, E., Chin, M.,
833 Starr, D., Sekiguchi, M., and Aires, F.: Introducing multi-sensor satellite radiance-based
834 evaluation for regional earth system modeling, *J. Geophys. Res.*, 119, 8450-8475,
835 doi:10.1002/2013JD021424, 2014.

836 Maurer, E. P., Wood, A. W., Adam, J. C., Lettenmaier, D. P., and Nijssen, B.: A long-term

837 hydrologically based dataset of land surface fluxes and states for the continuous United State,
838 *J. Clim.*, 15(22), 3,237-3,251, 2002.

839 Mu, M., Randerson, J. T., van der Werf, G. R., Giglio, L., Kasibhatla, P., Morton, D., Collatz, G.
840 J., DeFries, R. S., Hyer, E. J., Prins, E. M., Griffith, D. W. T., Wunch, D., Toon, G. C.,
841 Sherlock, V., and Wennberg, P. O.: Daily and 3-hourly variability in global fire emissions
842 and consequences for atmospheric model prediction of carbon monoxide, *J. Geophys. Res.*,
843 116, D24303, doi:10.1029/2011JD016245, 2011.

844 Neal, L. S., Dalvi, M., Folberth, G., McInnes, R. N., Agnew, P., O'Connor, F. M., Savage, N. H.,
845 and Tilbee, M.: A description and evaluation of an air quality model nested within global
846 and regional composition-climate models using MetUM, *Geosci. Model Dev.*, 10, 3941-3962,
847 doi:10.5194/gmd-10-3941-2017, 2017.

848 Peters-Lidard, C. D., Houser, P. R., Tian, Y., Kumar, S. V., Geiger, J., Olden, S., Lighty, L., Doty,
849 B., Dirmeyer, P., Adams, J., Mitchell, K., Wood, E. F., and Sheffield, J.: High-performance
850 Earth system modeling with NASA/GSFC's Land Information System, *Innovations in*
851 *Systems and Software Engineering*, 3, 157–165, 2007.

852 Peters-Lidard, C. D., Kemp, E. M., Matsui, T., Santanello, J. A., Kumar, S. V., Jacob, J. P., Clune,
853 T., Tao, W.-K., Chin, M., Hou, A., Case, J. L., Kim, D., Kim, K.-M., Lau, W., Liu, Y., Shi,
854 J., Starr, D., Tan, Q., Tao, Z., Zaitchik, B. F., Zavadsky, B., Zhang, S. Q., and Zupanski,
855 M.: Integrated modeling of aerosol, cloud, precipitation and land processes at satellite-
856 resolved scales. *Environmental Modeling & Software* 67, 149-159, 2015.

857 Rienecker, M. M., Suarez, M. J., Gelaro, R., Todling, R., Bacmeister, J., Liu, E., Bosilovich, M.
858 G., Schubert, S. D., Takacs, L., Kim, G.-K., Bloom, S., Chen, J., Collins, D., Conaty, A., da
859 Silva, A., Gu, W., Joiner, J., Koster, R. D., Lucchesi, R., Molod, A., Owens, T., Pawson, S.,
860 Pegion, P., Redder, C. R., Reichle, R., Robertson, F. R., Ruddick, A. G., Sienkiewicz, M.,
861 and Woollen, J.: MERRA - NASA's Modern-Era Retrospective Analysis for Research and
862 Applications, *J. Climate*, 24, 3624–3648, 2011.

863 Seo, J., Youn, D., Kim, J. Y., and Lee, H.: Extensive spatiotemporal analyses of surface ozone and
864 related meteorological variables in South Korea for the period 1999-2010, *Atmos. Chem.*
865 *Phys.*, 14, 6395-6415, doi:10.5194/acp-14-6395-2014, 2014.

866 Shi, J. J., Matsui, T., Tao, W.-K., Tan, Q., Peters-Lidard, C. D., Chin, M., Pickering, K., Guy, N.,
867 Lang, S., and Kemp, E. M.: Implementation of an aerosol-cloud microphysics-radiation
868 coupling into the NASA Unified WRF: Simulation results for the 6-7 August 2006 AMMA
869 Special Observing Period, *Q. J. R. Meteorol. Soc.*, doi:10.1002/qj.2286, 2014.

870 Stockwell, W. R., Middleton, P., Chang, J. S., and Tang, X.: The Second Generation Regional
871 Acid Deposition Model Chemical Mechanism for Regional Air Quality Modeling, *J.*
872 *Geophys. Res.*, 95, 16343-16367, 1990.

873 Tao, W.-K., Shi, J. J., Chen, S. S., Lang, S., Lin, P.-L., Hong, S.-Y., Peters-Lidard, C., and Hou,
874 A.: The impact of microphysical schemes on hurricane intensity and track, *Asia-Pacific J.*
875 *Atmos. Sci.*, 47, 1–16, 2011.

876 Tao, Z., Santanello, J. A., Chin, M., Zhou, S., Tan, Q., Kemp, E. M., and Peters-Lidard, C. D.:
877 Effect of land cover on atmospheric processes and air quality over the continental United
878 States – A NASA Unified WRF (NU-WRF) model study, *Atmos. Chem. Phys.*, 13, 6207-
879 6226, doi: 10.5194/acp-13-6207-2013, 2013.

880 Tao, Z., Yu, H., and Chin, M.: Impact of transpacific aerosol on air quality over the United States:
881 A perspective from aerosol-cloud-radiation interactions, *Atmos. Environ.*, 125, 48-60,
882 doi:10.1016/j.atmosenv.2015.10.083, 2016.

883 Tao, Z., Braun, S. A., Shi, J. J., Chin, M., Kim, D., Matsui, T., and Peters-Lidard, C. D.:
884 Microphysics and radiation effect of dust on Saharan air layer: An HS3 case study, *Mon. Wea.*
885 *Rev.*, 146, 1813-1835, doi:10.1175/MWR-D-17-0279.1, 2018.

886 Tie, X., Brasseur, G., and Ying, Z.: Impact of model resolution on chemical ozone formation in
887 Mexico City: application of the WRF-Chem model, *Atmos. Chem. Phys.*, 10, 8983-8995,
888 doi:10.5194/acp-10-8983-2010, 2010.

889 Valari, M. and Menut, L.: Does an increase in air quality model's resolution bring surface ozone
890 concentrations closer to reality?, *J. Atmos. Oceanic Tech.*, 25, 1955-1968,
891 doi:10.1175/2008JTECHA1123.1, 2008.

892 van der Werf, G. R., Randerson, J. T., Giglio, L., Collatz, G. J., Mu, M., Kasibhatla, P. S.,
893 Morton, D. C., DeFries, R. S., Jin, Y., and van Leeuwen, T. T.: Global fire emissions and the
894 contribution of deforestation, savanna, forest, agricultural, and peat fires (1997–2009),
895 *Atmos. Chem. Phys.*, 10, 11707-11735, doi:10.5194/acp-10-11707-2010, 2010.

896 Wang, W.-N., Cheng, T.-H., Gu, X.-F., Chen, H., Guo, H., Wang, Y., Bao, F.-W., Shi, S.-Y., Xu,
897 B.-R., Zuo, X., Meng, C., and Zhang, X.-C.: Assessing spatial and temporal patterns of
898 observed ground-level ozone in China, *Sci. Rep.*, 7, 3651, doi:10.1038/s41598-017-03929-
899 w, 2017.

900 Yu, Man: An assessment of urbanization impact on China by using WRF-Chem and configuration
901 optimization, PhD (Doctor of Philosophy) thesis, University of Iowa,
902 <https://doi.org/10.17077/etd.lzfu2tj8>, 2014.

903 Zhao, X. J., Zhao, P. S., Xu, J., Meng, W., Pu, W. W., Dong, F., He, D., and Shi, Q. F.: Analysis
904 of a winter regional haze event and its formation mechanism in the North China Plain, *Atmos.*
905 *Chem. Phys.*, 13, 5685-5696, doi:10.5194/acp-13-5685-2013, 2013.

906 Zou, Y., Wang, Y., Zhang, Y., and Koo, J.-H.: Arctic sea ice, Eurasia snow, and extreme winter
907 haze in China, *Sci. Adv.*, 3, e1602751, 2017.

908
909
910
911
912

913 Table 1. Information of Air Quality Observation Sites
 914

Site Name	Symbol	Longitude	Latitude	Altitude (m)	Setting
Baoding	BD	115.441	38.824	4	Urban
Beijing Tower	BJT	116.372	39.974	44	Urban
Chengde	CD	117.925	40.973	395	Urban
Caofeidian	CFD	118.442	39.270	11	Urban
Cangzhou	CZ	116.779	38.286	12	Urban
Datong	DT	113.389	40.089	1058	Urban
Gu An	GA	115.734	39.149	21	Rural
Hejian	HJ	116.079	38.423	66	Urban
Hengshui	HS	115.656	37.742	77	Urban
Langfang	LF	116.689	39.549	19	Urban
Lingshan	LS	115.431	39.968	116	Rural
Longtan Lake	LTH	116.430	39.870	31	Urban
Qian An	QA	118.800	40.100	54	Urban
Qinhuangdao	QHD	119.570	39.950	2.4	Urban
Shijiazhuang	SJZ	114.529	38.028	70	Urban
Shuangqing Road	SQL	116.338	40.007	58	Urban
Tanggu	TG	117.717	39.044	13	Urban
Tianjin	TJ	117.206	39.075	2	Urban
Tangshan	TS	118.156	39.624	14	Urban
Xianghe	XH	116.962	39.754	9	Suburban
Xinglong	XL	117.576	40.394	879	Rural
Yangfang	YF	116.126	40.147	78	Suburban
Yanjiao	YJ	116.824	39.961	26	Suburban
Zhangjiakou	ZJK	114.918	40.771	777	Urban
Zhuozhou	ZZ	115.988	39.460	48	Suburban

915
 916
 917
 918
 919
 920

Table 2. Comparisons of occurrences of exceedances of China's National Ambient Air Quality Standards between observations and simulations*

	Frequency	Class 1	Class 2	Obs.	45-km	15-km	5-km
CO	Hourly	10	10	1,150	0	0	0
O ₃	Hourly	160	200	3,684	24,807	10,283	9,880
NO _x	Hourly	250	250	9,009	14	520	3,003
SO ₂	Hourly	150	500	393	0	2	39
PM _{2.5}	24-hours	35	75	1,343	1,720	1,610	1,574
PM ₁₀	24-hours	50	150	2,834	2,067	1,617	1,676

921 * Class 1/2 standards are for rural/suburban-urban, respectively. Units are ppbm for CO, ppbv for O₃, NO_x,
 922 and SO₂, and µg m⁻³ for PM_{2.5} and PM₁₀.
 923
 924

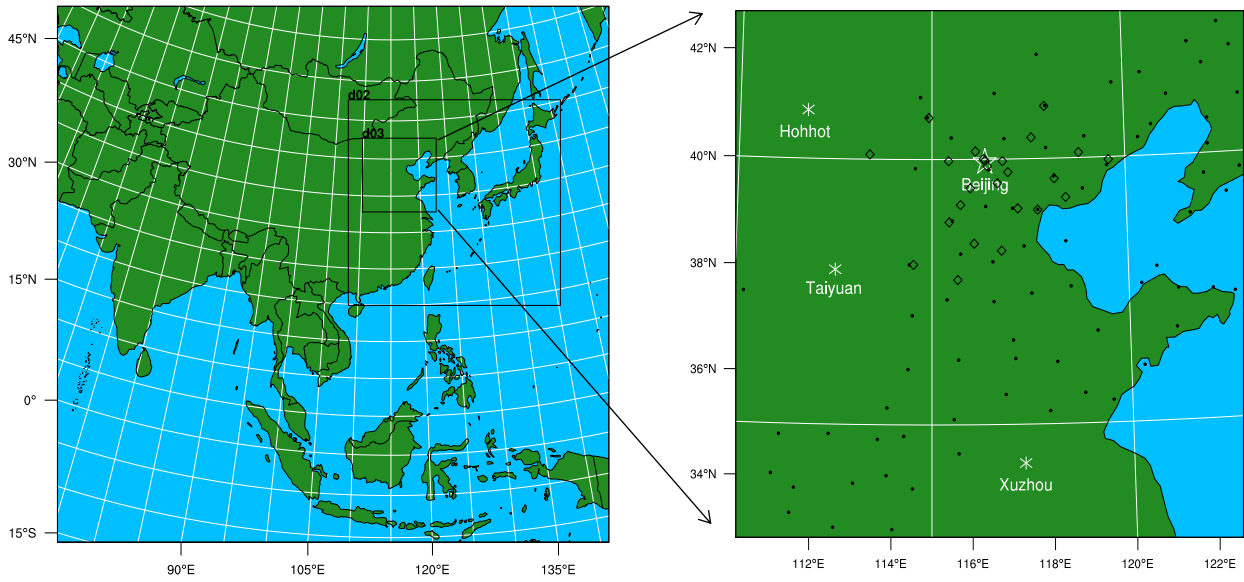
925
926
927

Table 3. Domain total emissions and average meteorology and air quality at various resolutions

Variables	Period	45-km	15-km	5-km
Biogenic Isoprene (tons)	Annual	740,562	869,317	862,199
Dust (tons)	Annual	2,431	4,485	3,910
Sea salt (tons)	Annual	548	1,287	1,417
Surface air temperature (K)	January	268	267	268
	July	300	299	299
Surface wind speed (m s ⁻¹)	January	2.92	2.73	2.51
	July	1.70	1.54	1.52
SWDOWN (W m ⁻²)	January	124	117	117
	July	249	242	250
PBLH (m)	January	333	338	331
	July	627	595	574
CWP (g m ⁻²)	January	4.34	11.3	11.1
	July	41.4	56.8	55.2
Surface O ₃ (ppbv)	January	37.5	39.4	39.5
	July	86.8	68.8	69.2
Surface NO _x (ppbv)	January	19.8	14.9	15.0
	July	9.03	8.32	7.96
Surface CO (ppmv)	January	0.600	0.521	0.526
	July	0.444	0.336	0.308
Surface SO ₂ (ppbv)	January	16.6	12.9	13.2
	July	10.2	6.55	6.23
Surface PM _{2.5} (μg m ⁻³)	January	70.9	59.8	61.0
	July	89.3	58.0	46.2
Surface PM ₁₀ (μg m ⁻³)	January	102	88.1	89.6
	July	108	74.9	60.3

928
929

930



931

932

933

934

935

936

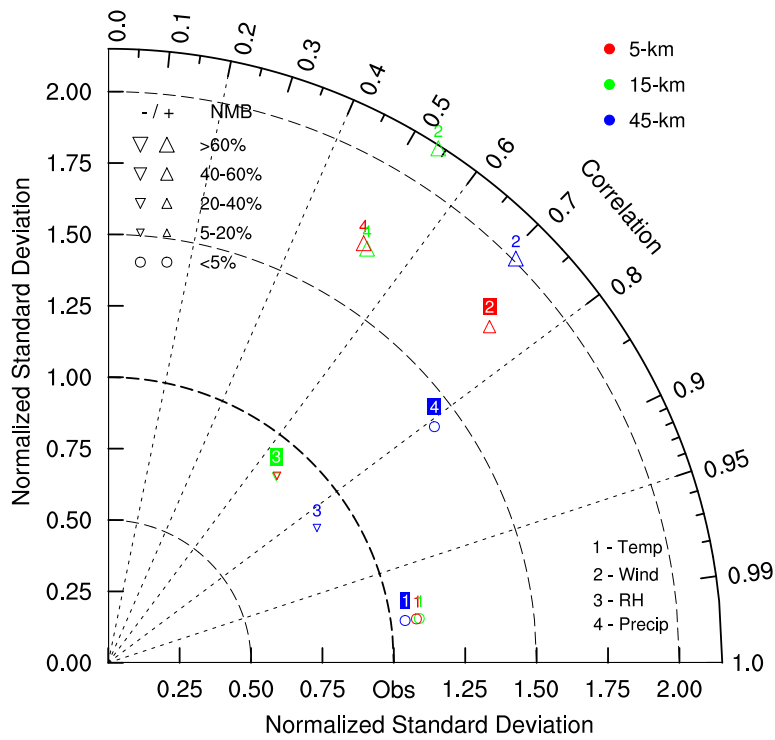
937

938

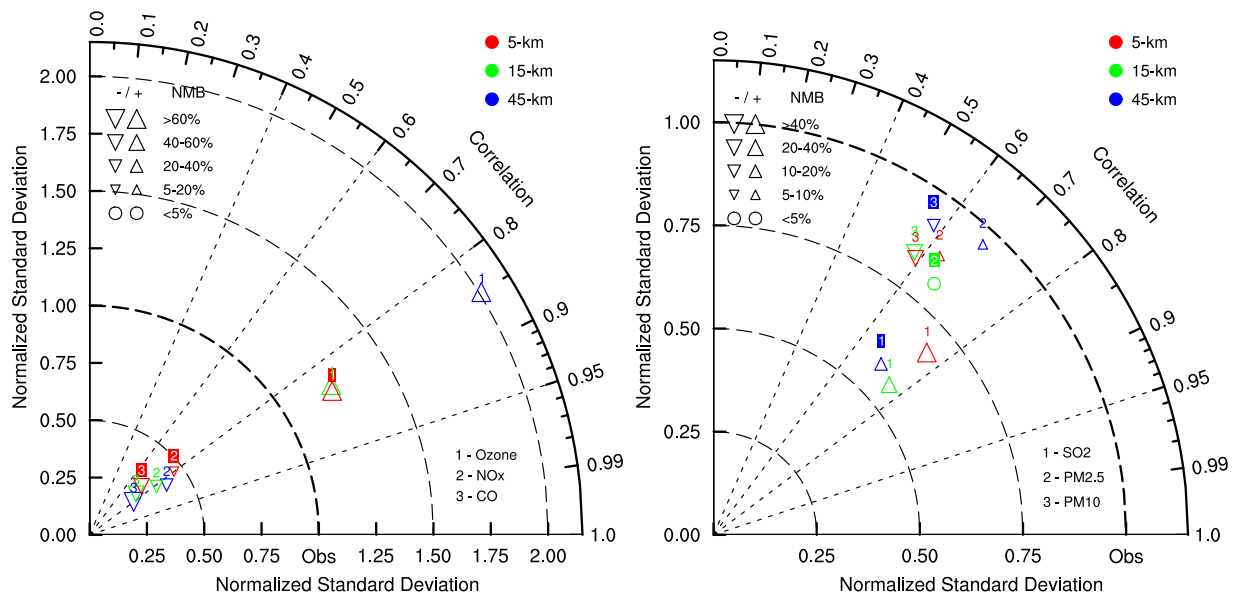
939

Figure 1. NU-WRF domain set-up. Left panel is the nested MICS-Asia domains; right panel is the enlarged NCP domain (d03) with diamonds representing the air quality monitoring sites and black dots denoting for the meteorological stations. Locations of four cities are marked for position reference.

940



941



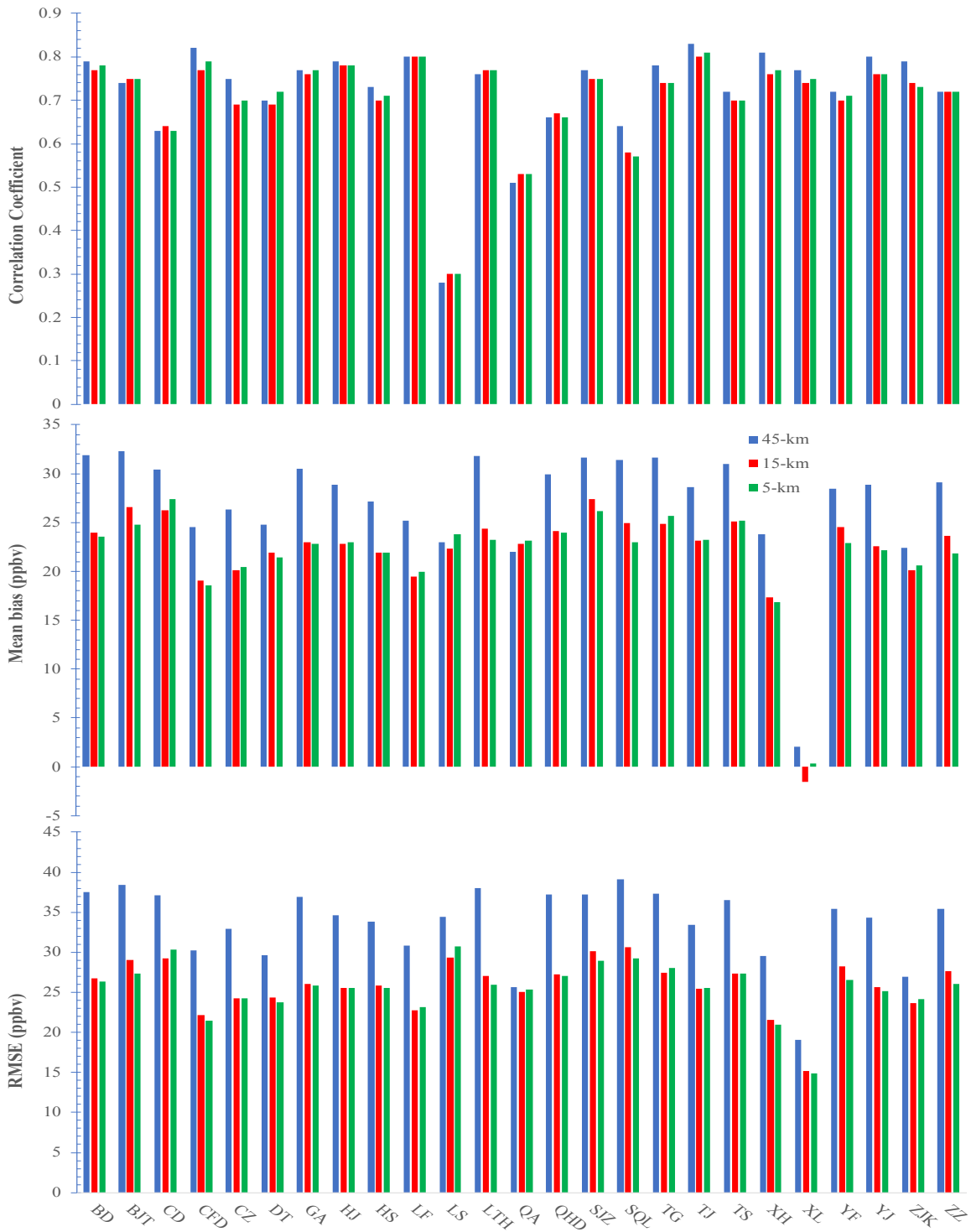
942

943

944 Figure 2. Taylor diagram for evaluations of NU-WRF performances on meteorology (top row) and
945 air quality (bottom row) simulations at three resolutions

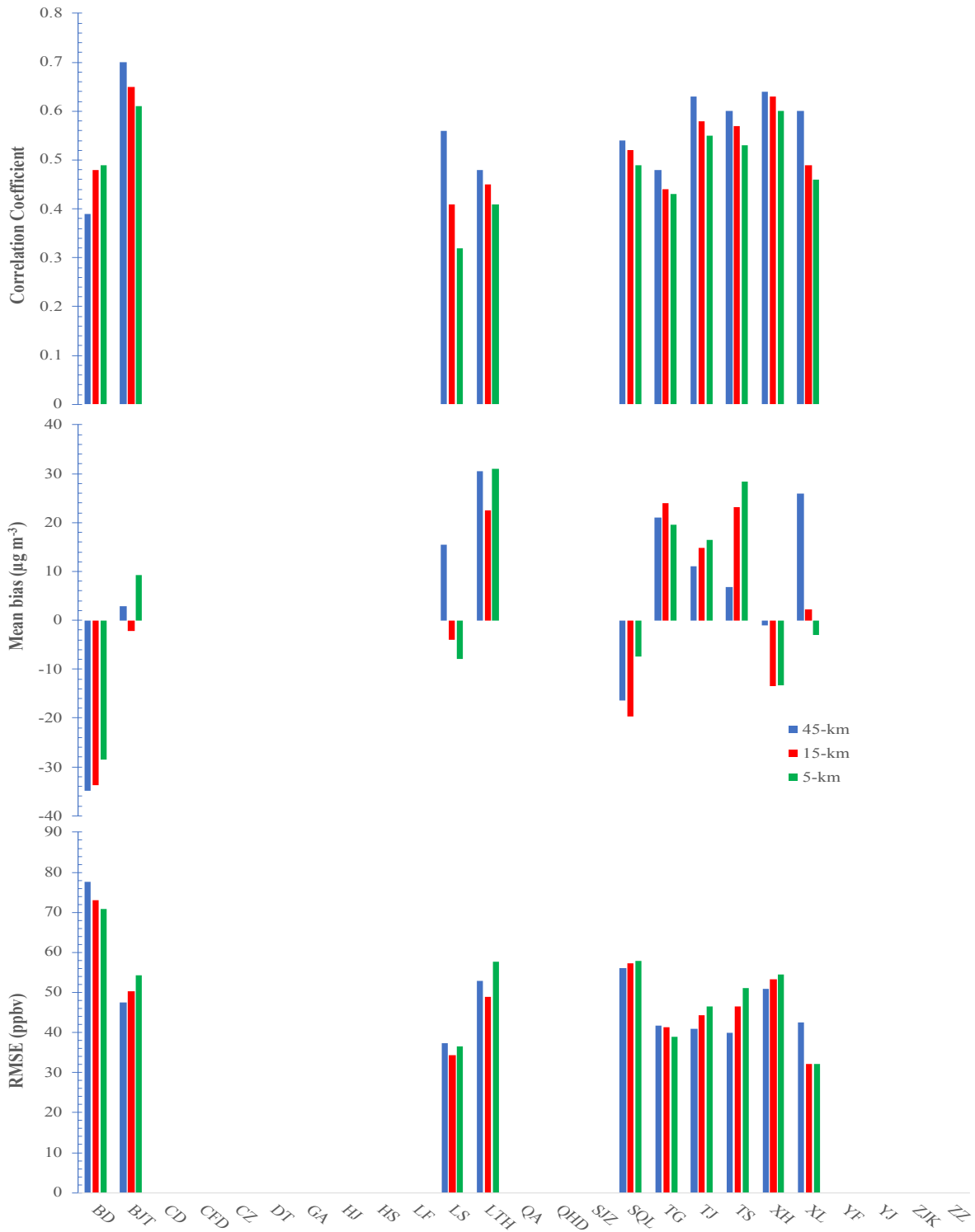
946

947



949
 950
 951
 952
 953

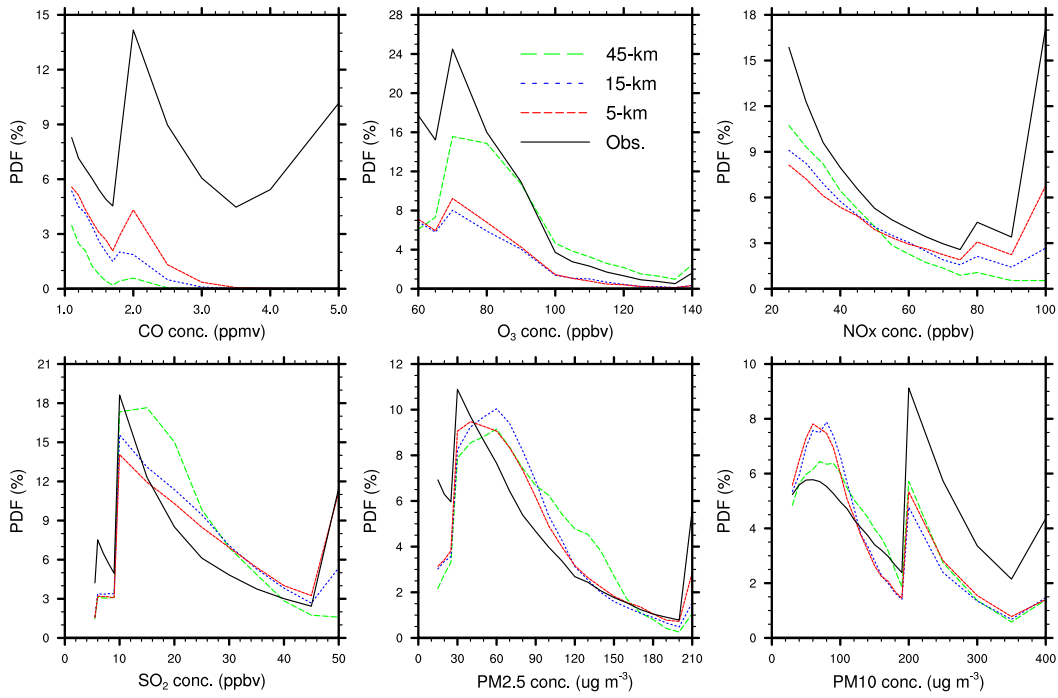
Figure 3. Comparisons of *MB*, *RMSE*, and correlation coefficient (*r*) of surface O₃ from different horizontal resolutions at each air quality monitoring site



955
 956
 957
 958
 959

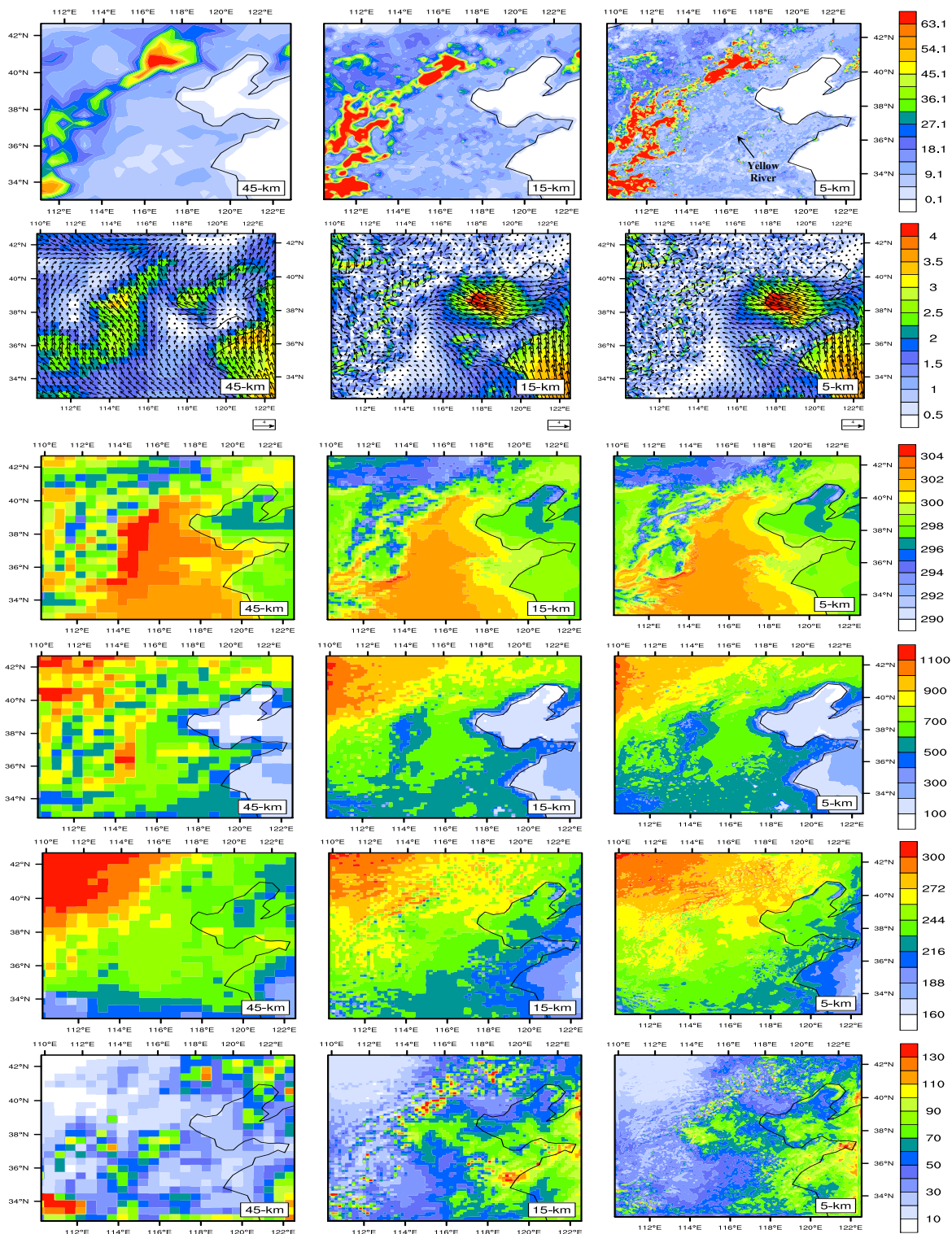
Figure 4. Comparisons of *MB*, *RMSE*, and correlation coefficient (*r*) of surface PM_{2.5} from different horizontal resolutions at each air quality monitoring site (blank space indicates no data are available)

960

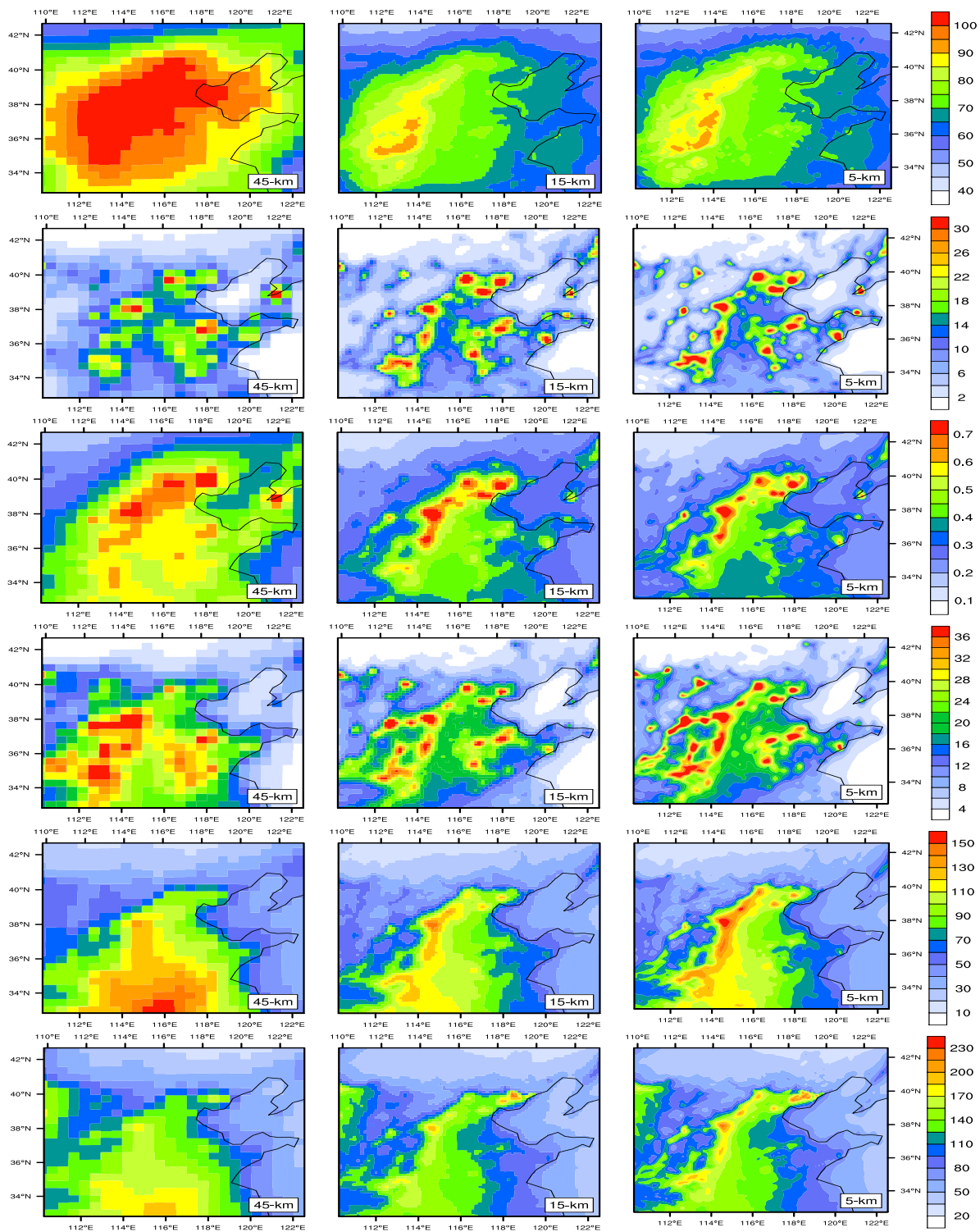


961
962
963
964

Figure 5. Probability density function (PDF) plots for hourly concentrations of surface air quality

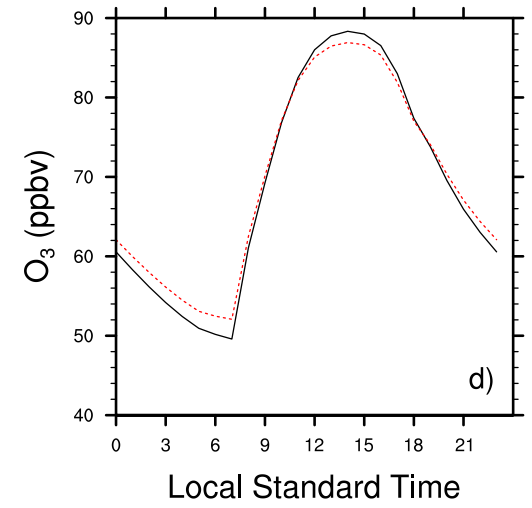
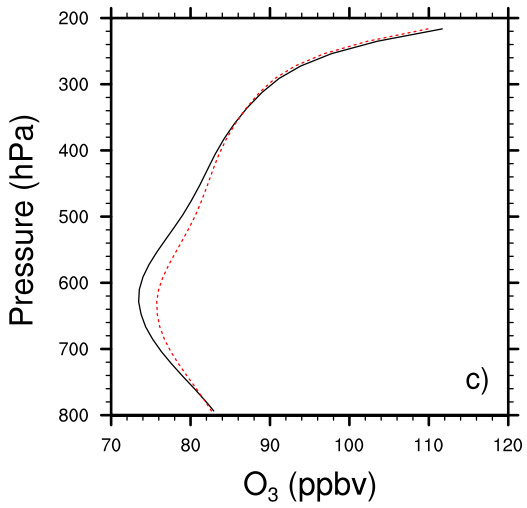
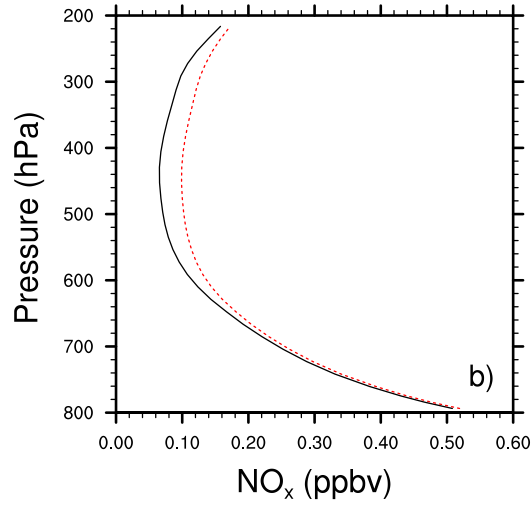
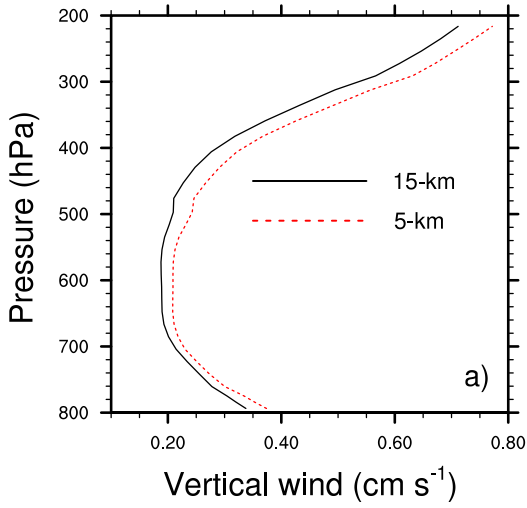


965
 966 Figure 6. Simulated emissions and July average meteorology from 3 grids: 1st row = isoprene
 967 emissions ($\text{mol km}^{-2} \text{hr}^{-1}$) from biogenic sources on a typical summer day; 2nd row = surface wind
 968 vector with the shade representing wind speed (m s^{-1}); 3rd row = surface air temperature (K); 4th
 969 row = PBLH (m); 5th row = SWDOWN (W m^{-2}); 6th row = CWP (g m^{-2}).
 970



971
 972
 973
 974
 975
 976

Figure 7. Simulated January (SO_2 , $\text{PM}_{2.5}$, and PM_{10}) and July (O_3 , NO_x , and CO) surface average air quality from 3 grids: 1st row = O_3 (ppbv); 2nd row = NO_x (ppbv) 3rd row = CO (ppmv); 4th row = SO_2 (ppbv); 5th row = $\text{PM}_{2.5}$ ($\mu\text{g m}^{-3}$); 6th row = PM_{10} ($\mu\text{g m}^{-3}$).



977
978
979
980

Figure 8. Domain average profiles of vertical wind, NO_x, and O₃ concentrations (Panels a~c) and domain average diurnal variations of surface O₃ over July